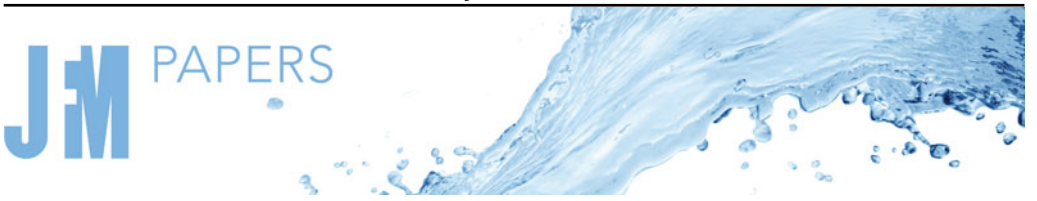
J. Fluid Mech. (2026), *vol.* 1029, A11, doi:10.1017/jfm.2026.11153



Elliptic approximation model revisited

Zhongxin Yang[1], **Xiang I.A. Yang**[2] **and Shiyi Chen**[3]

[1]College of Engineering, Peking University, Beijing, 100871, PR China

[2]Mechanical Engineering, Pennsylvania State University, State College, 16802, PA, USA

[3]Eastern Institute for Advanced Study, Eastern Institute of Technology, Ningbo, Zhejiang, 315200, PR China

Corresponding author: Zhongxin Yang, zhongxinyang@stu.pku.edu.cn

(Received 1 July 2025; revised 20 December 2025; accepted 5 January 2026)

The elliptic approximation (EA) – rooted in Taylor's frozen flow hypothesis, Kolmogorov's theory of small-scale turbulence, and the Kraichnan–Tennekes random sweeping hypothesis – remains a foundational framework for modelling spatiotemporal velocity correlations in incompressible wall-bounded turbulence. This study revisits the model's theoretical basis, and extends its applicability to velocity and temperature fluctuations in supersonic channel flows. First, we identify non-elliptic distortions in the viscous sublayer, and introduce a shear-induced acceleration that captures the observed deviation from the assumed constant convection velocity at large time separations. Next, we show that the inertial-range scalings underpinning the EA are not valid in regions where the model remains accurate; instead, its validity is supported by extended self-similarity between spatial and temporal structure functions. Finally, we conduct high-fidelity direct numerical simulations of compressible channel flows with fluctuating Mach numbers up to 0.8; our data confirm the robustness of the EA under supersonic conditions, and its effectiveness in characterising both velocity and temperature correlations. Together, these findings provide new theoretical insights into the spatiotemporal structure of wall-bounded turbulence, and broaden the operational envelope of the EA.

Key words: turbulence theory

1. Introduction

Spatiotemporal correlations quantify how fluctuations in a turbulent flow at one point in space and time relate to those at another. They are central to understanding the mechanisms of turbulence decorrelation, and have broad theoretical and practical relevance (He, Jin & Yang 2017). Fundamentally, these correlations provide a means of characterising the temporal evolution of spatial structures, which is essential for the development of turbulence theory. They also underpin a variety of closure models in turbulence,

© The Author(s), 2026. Published by Cambridge University Press.

https://doi.org/10.1017/jfm.2026.11153 Published online by Cambridge University Press

including the direct interaction approximation (Kraichnan 1961), the eddy-damped quasi-normal Markovian model (Orszag 1973), and several Eulerian-based closure frameworks (Cambon & Scott 1999).

Beyond their foundational role in turbulence theory and modelling, spatiotemporal correlations have widespread practical importance across several areas of fluid mechanics. In aeroacoustics, for example, the Lighthill acoustic analogy relates the intensity of sound radiated by turbulent flows to the underlying spatiotemporal structure of velocity fluctuations (Lighthill 1952). Accurate modelling of these correlations is therefore essential for predicting turbulence-generated noise (Wang, Freund & Lele 2006). In experimental fluid mechanics, spatiotemporal correlations also play a critical role. Due to the difficulty of simultaneously resolving fine-scale turbulence in both space and time, especially in high-Reynolds-number flows, experimentalists often rely on models to convert between temporal and spatial measurements (Ligrani & Bradshaw 1987; Vukoslavčević *et al.* 1991; Hutchins *et al.* 2009; Atkinson, Buchmann & Soria 2015). For instance, Taylor's frozen turbulence hypothesis (Taylor 1938) has long been used to infer spatial structures from time-resolved probe data. More refined spatiotemporal models now provide improved mappings that account for decorrelation effects and are increasingly used to interpret particle image velocimetry, hot-wire anemometry and laser Doppler velocimetry data (Del Alamo & Jiménez 2009). In this context, models of spatiotemporal correlations help to bridge the gap between limited experimental observables and the full dynamical structure of turbulent flows.

A particularly well-studied quantity in this context is the space–time correlation of streamwise velocity fluctuations in a homogeneous flow direction at statistically stationary conditions. This is commonly defined as

$$R_{uu}(r,\tau) = \langle u'(\boldsymbol{x},t)\, u'(\boldsymbol{x}+r\boldsymbol{e}_1, t+\tau)\rangle, \tag{1.1}$$

where $\boldsymbol{e}_1$ is the unit vector in the streamwise direction, r is the spatial separation, and τ is the temporal lag. For brevity, we denote this as $R(r,\tau)$. Here, $R(r,\tau)$ does not depend on x or t because of the assumed spatial homogeneity and temporal stationarity.

A number of models exist for $R(r,\tau)$. One of the earliest models of space–time correlation is based on Taylor's frozen turbulence hypothesis (Taylor 1938), which assumes that small-scale turbulent structures are convected unchanged at a mean velocity U_c, such that $R(r,\tau) = R(r - U_c\tau, 0)$. While Taylor's hypothesis captures the dominant convection of eddies, it fails to account for the decorrelation that occurs due to nonlinear interactions, large-scale sweeping, and distortion effects (Dennis & Nickels 2008; Moin 2009). To address these limitations, He & Zhang (2006) introduced the elliptic approximation (EA), which incorporates not only mean convection but also turbulent sweeping and distortion. The EA, derived from a Taylor series expansion of the space–time correlation function, combines the frozen flow hypothesis, Kolmogorov's similarity scaling (Kolmogorov 1941, 1991), and the Kraichnan–Tennekes random sweeping framework (Kraichnan 1964; Tennekes 1975). It relates space–time correlations to spatial correlations through an effective elliptical mapping defined by two characteristic velocities: a convection velocity governed by the local mean flow, and a sweeping velocity associated with turbulence intensity and shear rate (Zhao & He 2009). Other approaches have also been proposed. For example, Wilczek & Narita (2012) derived a random advection model incorporating mean flow based on Kraichnan's random sweeping hypothesis, yielding wavenumber–frequency spectra expressed as the instantaneous energy spectrum multiplied by a Gaussian frequency distribution. Wilczek *et al.* (2015*a*,*b*) demonstrated that the model captures essential features – Doppler shift and Doppler broadening – and established good agreement with numerical simulation

https://doi.org/10.1017/jfm.2026.11153 Published online by Cambridge University Press

data in the logarithmic layer of turbulent channel flows. And de Maré & Mann (2016) developed a spatiotemporal model by combining the Mann model (Mann 1994) with Kristensen's longitudinal coherence framework (Kristensen 1979), applicable to high-Reynolds-number turbulence. Lukassen *et al.* (2018) derived an analytical model based on the random sweeping hypothesis, expressing space–time correlations as a convolution of the spatial correlation with a temporal decorrelation kernel. Their model aligns with the classical Kovasznay–Corrsin conjecture (Phillips 2000). Towne, Lozano-Durán & Yang (2020) developed a resolvent-based estimation method to infer space–time flow statistics from limited known data, demonstrating its effectiveness in estimating flow characteristics in a low-Reynolds-number turbulent channel flow. Following Towne *et al.* (2020), Yang *et al.* (2020) systematically evaluated the performance of the resolvent-based estimation method, and found that the space–time energy spectra predicted are sensitive to the location of the reference plane. For comprehensive reviews of spatiotemporal correlations and modelling techniques, the reader is referred to Favre (1965), Wallace (2014), He *et al.* (2017) and Wu & He (2021*a*).

We consider the EA, which has been validated in a range of turbulent flows, including channel flows (He & Zhang 2006; Zhao & He 2009), turbulent Rayleigh–Bénard convection (He, He & Tong 2010; He & Tong 2011; Zhou *et al.* 2011), round jet (Zhang, Wan & Sun 2019) and turbulent boundary layers (Wang, Guan & Jiang 2014). Despite its success, several open questions remain regarding the applicability and theoretical foundations of the model. First, EA – like Taylor's hypothesis – assumes a constant convection velocity across the entire space–time domain. However, this assumption becomes increasingly inaccurate at large spatial separations and time delays. As the contribution from small-scale eddies diminishes with increasing r and τ, large-scale motions become dominant, and these possess different convection velocities. Del Alamo & Jiménez (2009) observed that small-scale eddies tend to convect with the local mean velocity, whereas larger, global modes travel at a nearly uniform speed proportional to the bulk flow velocity in channel flow. Second, the theoretical basis of the EA rests on assumptions that are strictly valid only within the inertial subrange. Specifically, the Kolmogorov similarity hypothesis (Kolmogorov 1941, 1991) provides the inertial-range scaling for the spatial energy spectrum, whereas the Kraichnan–Tennekes random sweeping hypothesis (Kraichnan 1964; Tennekes 1975) utilises this energy spectrum to derive the corresponding Eulerian frequency spectrum. Here, the random sweeping hypothesis does not assume inertial range, but due to Kolmogorov's similarity hypothesis, which assumes inertial range, the resulting Eulerian frequency spectrum is applicable to the inertial range only. Nevertheless, the EA often remains effective even at scales where viscous effects are non-negligible – a fact that lacks a clear theoretical explanation. Third, although the applicability of the EA has been extended to passive scalars (He *et al.* 2010; He & Tong 2011, 2014), existing discussions and validations of the EA are largely restricted to incompressible flows. Whether the model remains valid under compressible conditions, particularly at finite Mach numbers, has not been systematically explored.

This study addresses these open questions. We show that deviations from elliptic iso-correlation contours – termed 'non-elliptic effects' – in the viscous sublayer are attributable to viscous effects. A correction is proposed to account for these effects. Additionally, we demonstrate that the effectiveness of the EA does not hinge on strict inertial-range scaling; rather, it depends on the presence of extended self-similarity (ESS) between spatial and temporal correlations. Finally, we evaluate the applicability of the EA in compressible turbulence. We find that the model remains valid for describing the spatiotemporal correlations of both velocity and temperature fluctuations at finite Mach numbers.

https://doi.org/10.1017/jfm.2026.11153 Published online by Cambridge University Press

The remainder of this paper is organised as follows. In § 2, we revisit the theoretical derivation of the EA. The details of the direct numerical simulations (DNS) used in this study are provided in § 3. We then evaluate the key assumptions underlying the EA: in § 4.1, we examine deviations from ellipticity and propose a correction; in § 4.2, we test the Eulerian frequency spectrum derived from Kraichnan–Tennekes random sweeping hypothesis. The model's validity under compressible conditions is explored in § 4.3. Finally, conclusions are drawn in § 5.

2. The EA model

For completeness and to support the discussion in § 4, we summarise the EA and its derivation. Only the key steps are presented here; for detailed derivations, the reader is referred to He & Zhang (2006) and Zhao & He (2009).

Following He & Zhang (2006), the starting point is a Taylor expansion of the space–time correlation function $R(r, \tau)$ about $r = 0$, $\tau = 0$:

$$R(r, \tau) = R_0 + \left.\frac{\partial R}{\partial r}\right|_0 r + \left.\frac{\partial R}{\partial \tau}\right|_0 \tau + \left.\frac{\partial^2 R}{\partial r\, \partial \tau}\right|_0 r\tau + \frac{1}{2}\left[\left.\frac{\partial^2 R}{\partial r^2}\right|_0 r^2 + \left.\frac{\partial^2 R}{\partial \tau^2}\right|_0 \tau^2\right] + \cdots, \tag{2.1}$$

where the subscript 0 indicates evaluation at $r = 0$, $\tau = 0$. Due to the assumed spatial homogeneity and temporal stationarity, the first derivatives vanish: $\partial_r R|_0 = 0$ and $\partial_\tau R|_0 = 0$. Turbulence loses coherence over both space distance and time delay. Consider a spatial separation r_c such that the correlation at $(r_c, 0)$ equals that at (r, τ):

$$R(r, \tau) = R(r_c, 0). \tag{2.2}$$

Expanding the right-hand side yields

$$R(r, \tau) = R_0 + \left.\frac{\partial^2 R}{\partial r^2}\right|_0 r_c^2 + \cdots. \tag{2.3}$$

Comparing (2.1) and (2.3) up to second-order terms gives

$$r_c^2 = (r - U\tau)^2 + (V\tau)^2, \tag{2.4}$$

where

$$U = -\left.\frac{\partial^2 R}{\partial r\, \partial \tau}\right|_0 \left[\left.\frac{\partial^2 R}{\partial r^2}\right|_0\right]^{-1} \tag{2.5}$$

is the convection velocity, and

$$V^2 = \left.\frac{\partial^2 R}{\partial \tau^2}\right|_0 \left[\left.\frac{\partial^2 R}{\partial r^2}\right|_0\right]^{-1} - U^2 \tag{2.6}$$

is the sweeping velocity. Substituting (2.4) into (2.2) leads to

$$R(r, \tau) = R\left(\sqrt{(r - U\tau)^2 + (V\tau)^2}, 0\right), \tag{2.7}$$

which implies that space–time correlations decay across elliptical contours – hence the term 'elliptic approximation'. However, the derivation is strictly valid only for infinitesimal r and τ.

https://doi.org/10.1017/jfm.2026.11153 Published online by Cambridge University Press

Extending the EA to finite separations is non-trivial. A necessary (though not sufficient) condition is that the intercepts of a constant-R contour on the r- and τ-axes maintain a constant ratio. Zhao & He (2009) verified this condition by invoking Taylor's frozen turbulence hypothesis (Taylor 1938), Kolmogorov's similarity hypothesis (Kolmogorov 1941, 1991) and the Kraichnan–Tennekes random sweeping hypothesis (Kraichnan 1964; Tennekes 1975). First, according to Kolmogorov's theory and the random sweeping hypothesis, the second-order velocity structure function

$$D(r,\tau)=\left\langle \left|u_1'(x_1+r,t+\tau)-u_1'(x_1,t)\right|^2\right\rangle \tag{2.8}$$

has the following inertial-range scalings:

$$D(r,0)=C_K(\epsilon r)^{2/3}, \tag{2.9}$$

$$D(0,\tau)=C_K(\epsilon V_c\tau)^{2/3}, \tag{2.10}$$

where C_K is a constant, ϵ is the dissipation rate of turbulent kinetic energy, and V_c is a characteristic (constant) velocity. The structure function is related to the space–time correlation via

$$D(r,0)=2R(0,0)-2R(r,0), \tag{2.11}$$

$$D(0,\tau)=2R(0,0)-2R(0,\tau). \tag{2.12}$$

Next, let r_c and τ_c denote the spatial and temporal intercepts of a constant-R contour:

$$R(r_c,0)=R(0,\tau_c). \tag{2.13}$$

Finally, (2.9)–(2.13) together give

$$C_K(\epsilon r_c)^{2/3}=C_K(\epsilon V_c\tau_c)^{2/3}, \tag{2.14}$$

which simplifies to

$$\frac{r_c}{\tau_c}=V_c, \tag{2.15}$$

indicating that the ratio of spatial to temporal separation at equal correlation is constant in the inertial range.

To summarise, the EA in (2.7) provides a framework for relating temporal measurements at a single point to spatial correlations across the flow field. The model requires knowledge of two parameters: the convection velocity U, and the sweeping velocity V. In the original formulation, Zhao & He (2009) proposed estimating U from the local mean velocity, while V accounts for both shear-induced and random sweeping effects.

While the EA provides an approximation of space–time correlations using spatial correlations alone, two questions remain unresolved. First, the EA relies on inertial-range scaling arguments, which break down in the viscous sublayer. Second, the model was derived under the assumption of incompressibility. Its applicability to compressible flows at finite Mach numbers – where dilatational effects and acoustic modes may alter the correlation structure – is not well understood. These concerns motivate a closer examination of the model's validity in both near-wall and compressible regimes.

https://doi.org/10.1017/jfm.2026.11153 Published online by Cambridge University Press

3. The DNS details

3.1. *Governing equations*

The compressible Navier–Stokes equations are solved in a plane channel. The equations are written in index notation, with summation implied over repeated indices:

$$\frac{\partial \tilde{\rho}}{\partial t} + \frac{\partial (\tilde{\rho}\tilde{u}_j)}{\partial x_j} = 0, \tag{3.1}$$

$$\frac{\partial (\tilde{\rho}\tilde{u}_i)}{\partial t} + \frac{\partial (\tilde{\rho}\tilde{u}_i\tilde{u}_j)}{\partial x_j} = -\frac{\partial \tilde{p}}{\partial x_i} + \frac{\partial \tilde{\sigma}_{ij}}{\partial x_j} + f_i\delta_{i1}, \tag{3.2}$$

$$\frac{\partial (\tilde{\rho}\tilde{E})}{\partial t} + \frac{\partial (\tilde{\rho}\tilde{E}\tilde{u}_j)}{\partial x_j} = -\frac{\partial (\tilde{p}\tilde{u}_j)}{\partial x_j} + \frac{\partial (\tilde{u}_i\tilde{\sigma}_{ij})}{\partial x_j} - \frac{\partial \tilde{q}_j}{\partial x_j} + f_1\tilde{u}_1 - \phi, \tag{3.3}$$

where

$$\tilde{\sigma}_{ij} = 2\tilde{\mu}\tilde{S}_{ij} - \frac{2}{3}\tilde{\mu}\tilde{S}_{kk}\delta_{ij}, \quad \tilde{E} = C_V\tilde{T} + \frac{1}{2}\tilde{u}_i\tilde{u}_i, \quad \tilde{q}_j = -\tilde{\kappa}\frac{\partial \tilde{T}}{\partial x_j}. \tag{3.4}$$

Here, $\tilde{u}_i$ is the ith component of velocity in the Cartesian coordinate system x_i, t is time, $\tilde{p}$ is the thermodynamic pressure, $\tilde{\sigma}_{ij}$ is the viscous stress tensor, f_i is a uniform body force driving the flow (applied only in the streamwise direction), $\tilde{E}$ is the total energy per unit mass, $\tilde{q}_j$ is the heat flux vector, and ϕ represents a heat source term. The material properties include the dynamic viscosity $\tilde{\mu}$, thermal conductivity $\tilde{\kappa}$, and specific heat at constant volume C_V. The molecular Prandtl number is defined as $Pr = C_p\tilde{\mu}/\tilde{\kappa}$ and is set to 0.72 in the present simulations. Temperature dependence of the viscosity is modelled using Sutherland's law:

$$\tilde{\mu} = \mu_{ref}\left(\frac{\tilde{T}}{T_{ref}}\right)^{3/2}\frac{T_{ref}+S}{\tilde{T}+S}, \tag{3.5}$$

where μ_{ref} is the reference viscosity at reference temperature T_{ref}, and $S = 110.4$ K is Sutherland's constant. The ideal gas law is used to close the system:

$$\tilde{p} = \tilde{\rho}R\tilde{T}, \tag{3.6}$$

where R is the specific gas constant.

3.2. *Computational set-up*

The details of the DNS are summarised in table 1. The nomenclature of the cases follows the format M[$10 \times U_m/a_{ref}$]R[$Re/1000$]k. The bulk Reynolds number, Mach number, bulk Mach number and friction Reynolds number define the flow condition and are

$$Re = \frac{\rho_m U_m H}{\mu_w}, \quad Ma = \frac{U_m}{a_{ref}}, \quad Ma_b = \frac{U_m}{a_m}, \quad Re_\tau = \frac{\sqrt{\tau_w\rho_w}\,H}{\mu_w}, \tag{3.7}$$

with

$$\rho_m = \frac{1}{H}\int_0^H \langle\tilde{\rho}\rangle\,\mathrm{d}y, \quad U_m = \frac{1}{\rho_m H}\int_0^H \langle\tilde{\rho}\tilde{u}_1\rangle\,\mathrm{d}y. \tag{3.8}$$

Here, H is the channel half-height, the subscript m denotes a volume-averaged quantity, w indicates values at the wall, a_{ref} is the speed of sound at the reference temperature, and a_m is the speed of sound at the bulk temperature.

https://doi.org/10.1017/jfm.2026.11153 Published online by Cambridge University Press

https://doi.org/10.1017/jfm.2026.11153 Published online by Cambridge University Press

Case	Re	Ma	Ma_b	Re_τ	$N_x \times N_y \times N_z$	$\Delta x^+ \vert \Delta x^* \vert (\Delta x/\eta)$	$\Delta y_w^+ \vert \Delta y_w^* \vert (\Delta y_w/\eta_w)$	$\Delta y_c^+ \vert \Delta y_c^* \vert (\Delta y_c/\eta_c)$	$\Delta z^+ \vert \Delta z^* \vert (\Delta z/\eta)$	θ	$-B_q$
M04R03k	3000	0.4	0.40	186	$340 \times 129 \times 256$	7.2, 7.2, 4.5	0.5, 0.5, 0.3	6.0, 5.7, 1.5	4.8, 4.8, 3.0	−0.49	0.003
M08R03k	3000	0.8	0.77	197	$340 \times 129 \times 256$	7.3, 7.3, 4.7	0.5, 0.5, 0.3	6.4, 5.7, 1.5	4.8, 4.8, 3.1	−0.56	0.014
M15R03k	3000	1.5	1.30	218	$340 \times 129 \times 256$	7.9, 7.9, 5.1	0.5, 0.5, 0.3	7.0, 4.8, 1.3	5.3, 5.3, 3.4	−0.58	0.047
M30R05k	5000	3.0	1.94	446	$684 \times 256 \times 512$	8.2, 8.2, 5.1	0.5, 0.5, 0.3	7.2, 2.4, 0.7	5.5, 5.5, 3.4	−0.62	0.132
M80R27k*	26 600	8.0	4.42	416	$792 \times 288 \times 576$	6.6, 48.0, 5.3	0.4, 0.4, 0.3	6.0, 43.6, 4.1	4.5, 32.7, 3.6	0.61	0.022

Table 1. Computational parameters for the DNS. The suffix 'k' in case nomenclature denotes 'thousands' (kilo). The asterisk in the case M80R27k* indicates that this configuration incorporates a heating source term ϕ to maintain a prescribed bulk temperature, with wall temperature $10.09T_{ref}$, distinguishing it from other cases in the study. Grid resolution is characterised using three scalings. Wall-unit scaling (normalised by $\mu_w/\sqrt{\rho_w \tau_w}$) is given by Δx^+, Δy_w^+, Δy_c^+, Δz^+. Semi-local scaling (normalised by $\mu/\sqrt{\rho \tau_w}$) is represented by Δx^*, Δz^* for the largest spacings in the streamwise and spanwise directions, and by Δy_w^*, Δy_c^* for spacings at the wall and channel centreline, respectively. Kolmogorov scaling is indicated by $\Delta x/\eta$, $\Delta z/\eta$ for the largest spacings, and $\Delta y_w/\eta_w$, $\Delta y_c/\eta_c$ for spacings at the wall and centreline. Here, $\theta = (T_w - T_b)/(T_r - T_b)$ denotes the wall temperature parameter, with $T_r = T_e(1 + 0.5(\gamma - 1) r M_e^2)$ being the recovery temperature, and $-B_q = -q_w/(\rho_w C_p u_\tau T_w)$ is the heat flux coefficient.

The computational domain has dimensions $4\pi H \times 2H \times 2\pi H$, which is larger than the minimal channel used in earlier studies (Flores & Jiménez 2010; Lozano-Durán & Jiménez 2014). Domains of similar size have been employed in previous simulations of compressible channel flow (Coleman, Kim & Moser 1995; Morinishi, Tamano & Nakabayashi 2004; Chen *et al.* 2022). Grid points are clustered in the wall-normal (y) direction and uniformly distributed in the streamwise (x) and spanwise (z) directions. The first off-wall grid point satisfies $\Delta y_w^+ \leqslant 0.5$, and the wall-normal spacing at the channel centreline is $\Delta y_c^+ \lesssim 7.2$. The streamwise and spanwise grid spacings are $\Delta x^+ \lesssim 8$ and $\Delta z^+ \lesssim 5.5$, respectively. These resolutions comply with established DNS guidelines (Kim, Moin & Moser 1987; Oliver *et al.* 2014) and align with those used in recent compressible flow simulations (Modesti, Bernardini & Pirozzoli 2015; Yao & Hussain 2020; Zhang, Song & Xia 2023). Grid resolution is also reported in two additional scalings: semi-local units and Kolmogorov scaling. The largest grid spacings scaled by semi-local units are $\Delta x^* = 48.0$ and $\Delta z^* = 32.7$ in the streamwise and spanwise directions, respectively. These relatively large values result from the low temperature at the channel centreline – a situation that has been observed in hypersonic boundary layer flows (Zhang, Duan & Choudhari 2018; Huang, Duan & Choudhari 2022). Nevertheless, the grid resolution remains well within the grid resolution requirements for DNS, as is clear when it is expressed in Kolmogorov units. Although finer grids are necessary to capture rare intermittent events, the present resolution is sufficient to accurately resolve first- and second-order statistics (Yang *et al.* 2021; Chen *et al.* 2023), which are the primary focus of this study.

The boundary conditions are periodic in the streamwise (x) and spanwise (z) directions. The walls are no-slip and isothermal. The wall temperature is set to $T_w = T_{ref}$ for all cases except M80R27k*, which uses tailored wall temperature $10.09T_{ref}$. The reference temperature is $T_{ref} = 273$ K for all cases except M80R27k*, where it is 100 K. We set $H = 1$ and $\rho_m = 1$ in our DNS, and vary the viscosity μ_w and the driving force f_1 to control the Reynolds number Re and the Mach number Ma. In this channel configuration, all viscous heating is removed through the walls, resulting in a mean temperature gradient from the wall to the centre of the channel. At high Mach numbers, this gradient can significantly raise the centreline temperature, thereby increasing the viscosity and potentially causing relaminarisation. To mitigate this effect, we follow the work of Yu *et al.* (2019, 2020) and introduce a cooling source term ϕ in the energy equation (3.3) to regulate the bulk temperature. For case M80R27k*, the bulk temperature is set to $T_b/T_{ref} = 3.272$. The relevant aerodynamic heating parameters are also summarised in table 1. For each case, the heat flux coefficient $-B_q = -q_w/(\rho_w C_p u_\tau T_w)$ and wall temperature parameter $\theta = (T_w - T_b)/(T_r - T_b)$ are reported. Here, $T_r = T_e(1 + 0.5(\gamma - 1)rM_e^2)$ denotes the recovery temperature, with $r = 0.89$ being the recovery factor, and the subscript e referring to properties at the channel centreline. In the four cases without cooling, θ exhibits negative values due to the bulk temperature exceeding the wall temperature. In contrast, case M80R27k* shows the opposite behaviour, with significant cooling causing the bulk temperature to fall below the wall temperature. The heat flux coefficient generally increases with Mach number among the four typical cases without cooling, reaching the value 0.132 in case M30R05k. However, in case M80R27k*, this coefficient is even lower than that in the lower-Mach-number case M30R05k.

Calculations are performed using the OpenCFD-SC solver (Li *et al.* 2010), a high-order finite-difference code validated for compressible turbulence. Further details of the solver are available in previous studies (Liang & Li 2015; Xu *et al.* 2021; Yu & Xu 2021; Zhang *et al.* 2023). Here, we briefly summarise its key features. Convective terms are discretised using a seventh-order weighted essentially non-oscillatory (WENO) scheme,

https://doi.org/10.1017/jfm.2026.11153 Published online by Cambridge University Press

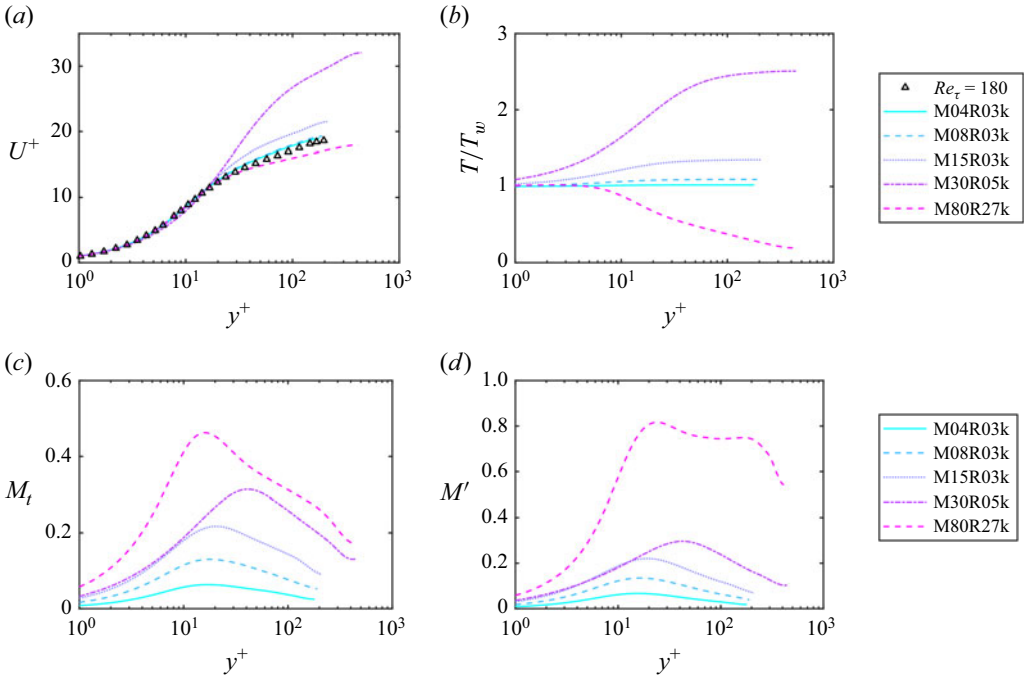


Figure 1. (*a*) Mean velocity profiles. (*b*) Mean temperature profiles. (*c*) Turbulent Mach number. (*d*) Fluctuating Mach number. The black symbols in (*a*) are reference incompressible channel flow data at $Re_\tau = 180$ (Modesti & Pirozzoli 2016).

and viscous terms with an eighth-order central difference scheme, and time integration is performed using a third-order explicit Runge–Kutta method. To ensure numerical stability at high Mach numbers, explicit filtering is applied to remove high-wavenumber oscillations (Bogey & Bailly 2004; Li, Fu & Ma 2006).

A total of 500 flow field snapshots are collected at intervals of $0.05H/U_m$, providing sufficiently fine temporal resolution to enable accurate analysis of spatiotemporal correlations. This temporal resolution has been demonstrated to be effective in previous studies (He & Zhang 2006; Wu & He 2021*b*; Yang & Yang 2022). Although the spatiotemporal correlation is defined in physical space, we leverage the periodicity in the streamwise direction to accelerate computations using fast Fourier transforms.

3.3. *Flow statistics*

Although the primary focus of this study is the spatiotemporal correlation of turbulence, we first present mean flow statistics to provide context for interpreting compressibility and Mach number effects.

Figure 1(*a*) shows the mean velocity profiles for all simulated cases. The $Re_\tau = 180$ incompressible channel flow (Modesti & Pirozzoli 2016) is also included for comparison. Case M04R03k, which is at the friction Reynolds number 180, closely follows the incompressible profile. As the Mach number increases, the mean velocity profiles progressively deviate from the incompressible law of the wall – except in case M80R27k*. Despite its high Mach number, M80R27k* exhibits a profile that remains relatively close to the incompressible reference. Figure 1(*b*) presents the corresponding mean temperature distributions. In cases without cooling, higher Mach numbers result in a stronger temperature difference between the channel centreline and the wall.

https://doi.org/10.1017/jfm.2026.11153 Published online by Cambridge University Press

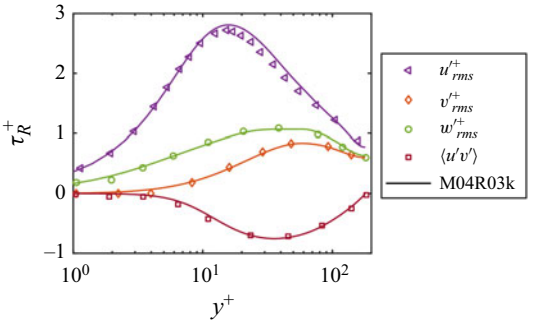


Figure 2. The distributions of root mean square fluctuating velocity and Reynolds shear stress for case M04R03k (lines) and its strictly incompressible counterpart (symbols) at friction Reynolds number $Re_\tau = 180$ (Modesti & Pirozzoli 2016).

This temperature contrast increases from $(T_c - T_w)/T_w = 0.02$ in M04R03k to 1.5 in M30R05k. By contrast, M80R27k* – due to the presence of a cooling source – exhibits an inverted temperature profile, with the centreline temperature lower than that at the wall. Figure 1(*c*,*d*) display the turbulent Mach number M_t and fluctuating Mach number M', respectively, defined as

$$M_t = \frac{\langle u_i'' u_i'' \rangle^{1/2}}{\langle c \rangle}, \quad M' = \sqrt{\left\langle \left(\frac{\sqrt{\tilde{u}_i \tilde{u}_i}}{c} - \left\langle \frac{\sqrt{\tilde{u}_i \tilde{u}_i}}{c} \right\rangle \right)^2 \right\rangle}. \tag{3.9}$$

These metrics characterise the intensity of turbulent fluctuations relative to the local speed of sound c. Both M_t and M' increase with Mach number, as expected. For cases without cooling, their spatial distributions are similar: peak magnitudes and locations align, and shift away from the wall with increasing Mach number. M80R27k* again shows distinct behaviour – M_t peaks at approximately 0.5 in the buffer layer ($y^+ \approx 18$), and M' exhibits a secondary peak in the outer region. This secondary peak, though uncommon in channel flows (Zhang *et al.* 2023), has been reported in hypersonic turbulent boundary layers (Duan, Beekman & Martin 2011). Finally, note that in M04R03k, both M_t and M' remain below 0.05, indicating negligible compressibility effects. This is further corroborated in figure 2, which shows that the root mean square fluctuating velocity and Reynolds shear stress profiles closely match those of the incompressible reference.

We also present a budget analysis for the energy. For a plane channel, the ensemble-averaged energy equation (3.3) simplifies to

$$\frac{\partial \langle -\tilde{\rho} u_i'' h_0'' \rangle}{\partial x_i} + \left\langle \tilde{u}_j \frac{\partial \tilde{\sigma}_{ij}}{\partial x_i} \right\rangle + \left\langle \tilde{\sigma}_{ij} \frac{\partial \tilde{u}_i}{\partial x_j} \right\rangle + \frac{\partial \langle -\tilde{q}_i \rangle}{\partial x_i} + \langle f_1 \tilde{u}_1 \rangle + \langle -\phi \rangle = 0, \tag{3.10}$$

where h_0'' is the fluctuation of total enthalpy. In the near-wall region, the energy balance is dominated by the interplay between viscous dissipation and wall heat conduction, which nearly offset each other. In the buffer layer, the dynamics becomes more complex as turbulent transport and viscous work both contribute appreciably to the energy transfer. Further away, in the outer layer, the balance depends on the cooling condition: without cooling, the body force work is mainly compensated by turbulent total enthalpy transport, whereas with cooling, it is offset by both the imposed cooling and turbulent transport.

https://doi.org/10.1017/jfm.2026.11153 Published online by Cambridge University Press

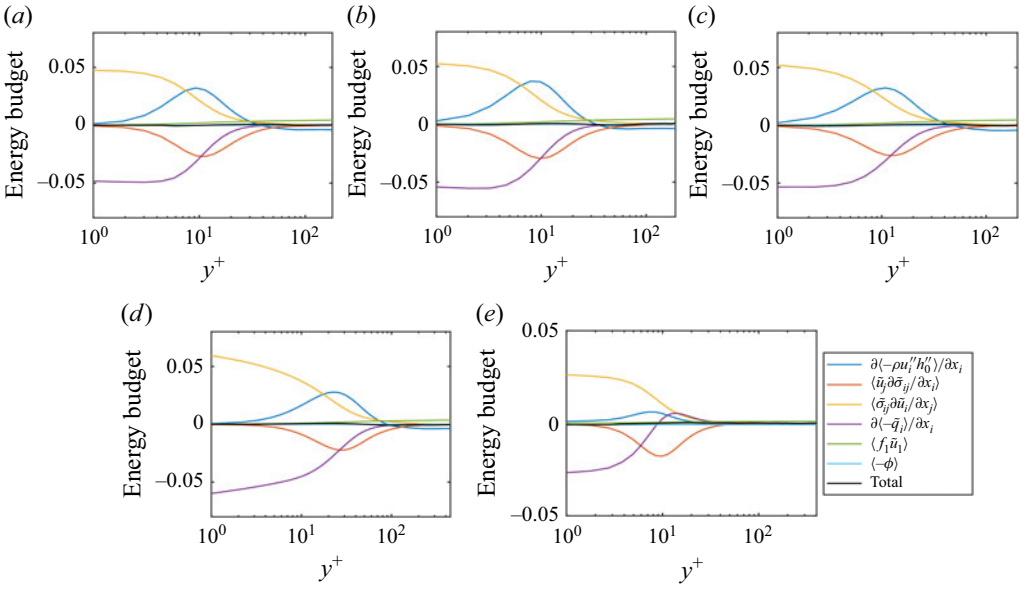


Figure 3. Energy budget analysis for (*a*) M04R03k, (*b*) M08R03k, (*c*) M15R03k, (*d*) M30R05k and (*e*) M80R27k*. All terms are normalised by $\rho_m U_m^3/H$.

4. Results

We assess the EA as defined in (2.7), and revisit its derivation. The convection velocity U and sweeping velocity V in (2.7) are extracted directly from DNS data, in contrast to Zhao & He (2009), who derived analytical expressions of these parameters from the Navier–Stokes equations under high-Reynolds-number, isotropic turbulence assumptions. Our approach allows us to isolate and evaluate the structural validity of the model itself.

This rest of this section is organised as follows. In § 4.1, we evaluate the assumption of a constant convection velocity at large spatial and temporal separations, demonstrating that U becomes scale-dependent due to shear effects. A correction is proposed to account for this variation. In § 4.2, we examine the validity of the inertial-range scalings in (2.9) and (2.10). Although these scalings break down near the wall, we show that the EA remains valid due to the presence of ESS. Finally, in § 4.3, we test the applicability of the EA to compressible flows and temperature fluctuations at finite Mach numbers. We find that the correction introduced in § 4.1 remains effective, and that ESS continues to hold for both velocity and temperature correlations under compressible conditions.

4.1. *Convection velocity*

The EA, like Taylor's hypothesis, assumes a constant convection velocity across all scales. To evaluate this assumption, we examine the spatiotemporal correlation structure in the low-Mach-number case M04R03k, focusing on the viscous sublayer and regions of large spatial separation r and time delay τ.

If the convection velocity were truly constant, then the principal axes of the iso-correlation contours would exhibit uniform inclination angles across all values of τ^+. Equivalently, for a time delay τ^+, the peak location Δx_p^+ of the correlation function $R(\Delta x^+, \tau^+)$ would scale linearly with τ^+.

Figure 4(*a–c*,*f–h*) illustrate this behaviour in the near-wall region ($y^+ = 1.9$, 5.1, 17.7). At small τ^+, the peak displacement Δx_p^+ varies linearly with τ^+ (figure 4*f–h*),

https://doi.org/10.1017/jfm.2026.11153 Published online by Cambridge University Press

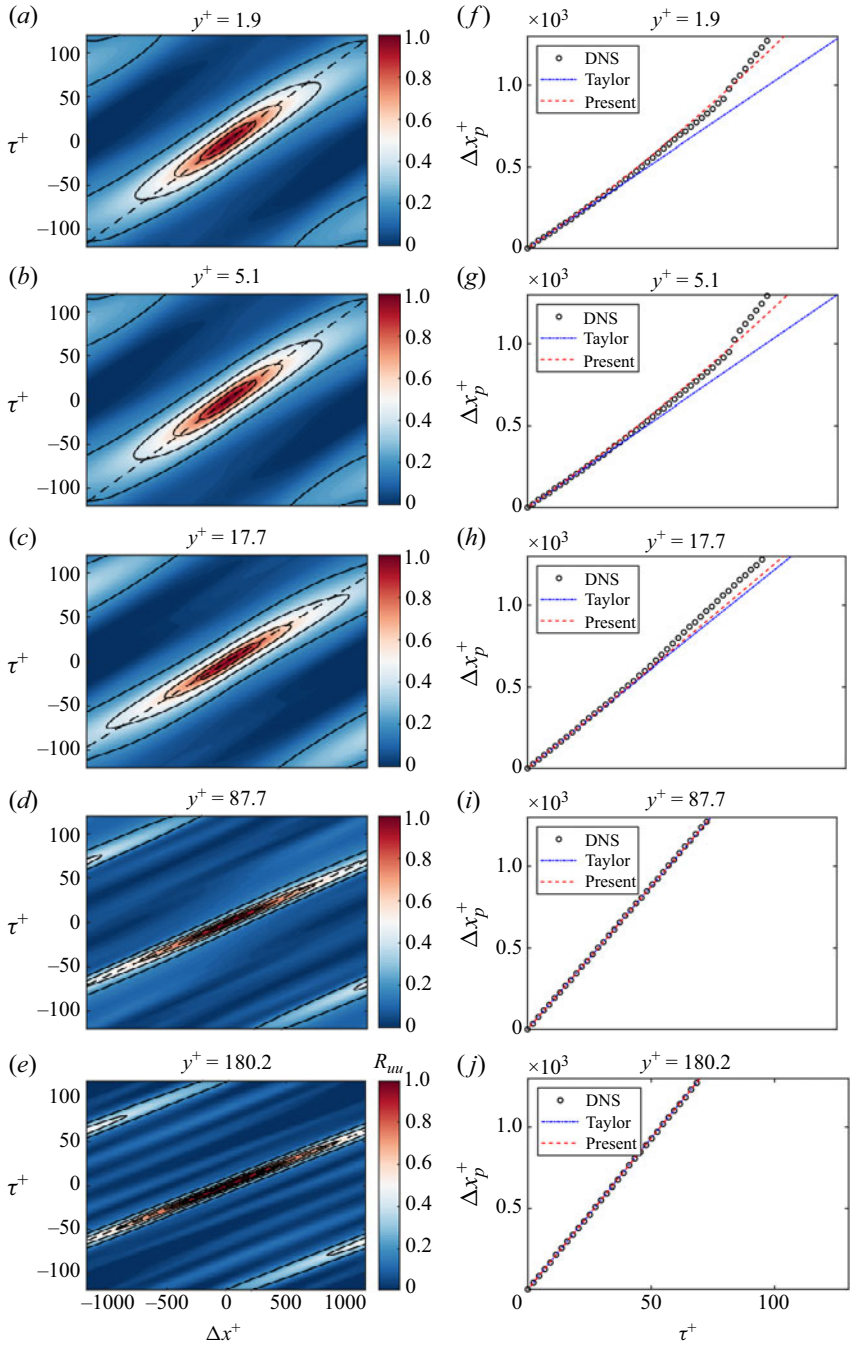


Figure 4. Spatiotemporal correlation in the low-Mach-number case M04R03k. (*a–e*) Iso-correlation contours at five wall-normal locations: (*a*,*f*) $y^+ = 1.9$, (*b*,*g*) $y^+ = 5.1$, (*c*,*h*) $y^+ = 17.7$, (*d*,*i*) $y^+ = 87.7$, and (*e*,*j*) $y^+ = 180.2$. Dashed lines indicate the inclination of the principal axis near the origin. (*f–j*) Evolution of the correlation peak location Δx_p^+ with increasing τ^+ at corresponding wall-normal positions. The Taylor hypothesis assumes constant convection velocity, whereas the present study employs the modified convection velocity defined in (4.3). Contour levels are $R = 0.8,\ 0.6,\ 0.4,\ 0.2$.

https://doi.org/10.1017/jfm.2026.11153 Published online by Cambridge University Press

consistent with a constant convection velocity at short time delays. However, at larger τ^+, the iso-correlation contours tilt progressively towards the Δx^+-axis (figure 4*a–c*), indicating an apparent increase in convection velocity over time. This deviation arises because Taylor's hypothesis assumes that advection dominates the evolution of turbulent structures; but additional mechanisms – such as convective acceleration, pressure gradients and viscous diffusion – become significant near the wall (Geng *et al.* 2015). These effects contribute to the breakdown of the constant convection velocity assumption in the near-wall region.

Figure 4(*d*,*e*,*i*,*j*) show results for the logarithmic and outer layers ($y^+ = 87.7,\ 180.2$). Here, the contour orientation remains largely invariant with τ^+, and the peak position Δx_p^+ scales linearly with τ^+, consistent with a constant convection velocity. These observations support the validity of the assumption that the influence of viscous and shear effects is small.

The breakdown of the constant convection velocity in the viscous sublayer is attributed to strong shear and viscous effects. Del Alamo & Jiménez (2009) formulated the convection velocity as a weighted integral of the phase velocity across wavenumbers:

$$U \sim \int c_u(k)\,|\hat{u}(k)|^2\,k^2\,\mathrm{d}k. \tag{4.1}$$

This implies convection is dominated by high-wavenumber modes – which decorrelate faster than low-wavenumber modes (Sanada & Shanmugasundaram 1992) – causing their spectral contribution to the correlation to diminish rapidly. Consequently, the convection velocity exhibits spatiotemporal variation due to significant phase-velocity differences between high- and low-wavenumber modes near the wall (Del Alamo & Jiménez 2009). To account for this, we introduce a shear-induced acceleration a_S. By dimensional analysis, this acceleration can only depend on the kinematic viscosity ν and the local mean shear $\partial\langle\tilde{u}_1\rangle/\partial y$ in the wall layer, and is

$$a_S = C\left[\nu\left(\frac{\partial\langle\tilde{u}_1\rangle}{\partial y}\right)^3\right]^{1/2}, \tag{4.2}$$

where $C = 0.021$ is a model constant obtained from DNS. The modified convection velocity is then given by

$$U_c = U + a_S\,|\tau|, \tag{4.3}$$

where U is the base convection velocity defined in (2.5), and U_c incorporates shear-induced effects. Equation (4.3) implies that this correction is most significant in the viscous sublayer, where the shear rate is highest. To evaluate the proposed correction, we compare DNS measurements of the peak correlation location Δx_p^+ with predictions from both the original EA and the modified formulation in (4.3), across wall-normal positions $y^+ = 1.9$, 5.1, 17.7, 87.7 and 180.2. Results are shown in figure 4(*f–j*). In the near-wall region (low y^+), the modified model more accurately captures the delayed shift of the correlation peak at large τ^+, outperforming the original EA formulation. This highlights the role of shear-induced acceleration in improving spatiotemporal correlation predictions near the wall. Additional validation under compressible conditions is presented in § 4.3.

We wish to emphasise that the objective of this section is not to propose a superior alternative to the existing EA model, but to identify and verify the physical mechanism that limits the standard model's accuracy in capturing peak shifts. The proposed correction serves to validate this physical insight, while maintaining the established EA framework. It should also be noted that the present model does not distinguish between turbulent

https://doi.org/10.1017/jfm.2026.11153 Published online by Cambridge University Press

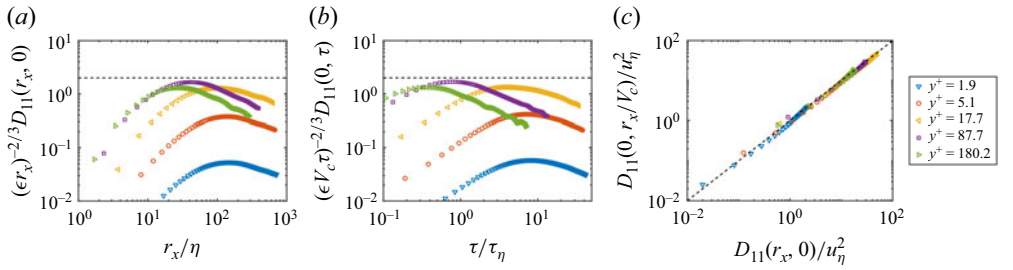


Figure 5. Second-order streamwise velocity structure functions for the low-Mach-number case M04R03k. (*a*) Spatial structure function $D_{11}(r_x, \tau = 0)$ pre-multiplied by $(\epsilon r_x)^{-2/3}$. (*b*) Temporal structure function $D_{11}(r_x = 0, \tau)$ pre-multiplied by $(\epsilon V_c \tau)^{-2/3}$. The dashed lines in (*a,b*) correspond to $C_K = 2$ (Pope 2001). (*c*) Temporal structure function re-plotted using r_x / V_c as the abscissa and compared to the spatial structure function. The dashed line denotes identity.

scales. Scale-dependent analyses can be found in e.g. Wills (1964) and Del Alamo & Jiménez (2009). Wills (1964) examined wavelength-dependent convection velocities using space–time energy spectra, while Del Alamo & Jiménez (2009) proposed a method for estimating the convection velocity of individual modes in turbulent shear flows based on temporal information and derivatives of the velocity signal. These approaches offer a more detailed characterisation of scale-dependent convection. However, compared to spatiotemporal correlation models such as Taylor's hypothesis and the EA, they require more extensive calibration and therefore are outside the current scope of the paper.

4.2. *Revisiting (2.9) and (2.10)*

As outlined in § 2, the validity of the EA at finite spatial separations and temporal delays relies on the inertial-range scalings of the second-order structure functions in (2.9) and (2.10). These scalings are traditionally associated with Kolmogorov's similarity hypothesis and the Eulerian frequency spectrum derived from the Kraichnan–Tennekes random sweeping hypothesis. In this subsection, we re-examine both scalings and demonstrate that although neither holds strictly across extended ranges, the EA remains valid due to the presence of ESS.

We focus again on the low-Mach-number case M04R03k. Figure 5(*a*) shows the spatial second-order streamwise velocity structure function, pre-multiplied by $(\epsilon r_x)^{-2/3}$. Similarly, figure 5(*b*) shows the temporal structure function, pre-multiplied by $(\epsilon V_c \tau)^{-2/3}$, where V_c is the characteristic velocity in (2.10), and $u_\eta = (\nu\epsilon)^{1/4}$, $\eta = (\nu^3/\epsilon)^{1/4}$ and $\tau_\eta = (\nu/\epsilon)^{1/2}$ are the Kolmogorov velocity, length and time scales, respectively. In regions where the inertial-range scalings hold, these compensated plots should display a plateau. However, as is evident from both plots, the inertial range, if one can argue that it exists, is extremely narrow – even at the channel centre – indicating that the classical spatial and temporal scaling laws are not valid under the current low-Reynolds-number conditions. However, the present work and prior work (e.g. He & Zhang 2006) demonstrate that the EA successfully reconstructs the spatiotemporal correlation function at large spatial separations (r) and time delays (τ).

To resolve this apparent contradiction, we revisit the derivation of the EA. Equations (2.9) and (2.10) are invoked in the derivation of (2.15). However, notice that the validity of (2.15) does not require the structure functions to follow the strict $r_x^{2/3}$ or $\tau^{2/3}$ scalings. Instead, it only requires that the space and time structure functions exhibit similar scaling under a linear transformation between r_x and τ. This condition is satisfied if the relationship between space and time follows the principle of ESS (Benzi *et al.* 1993,

https://doi.org/10.1017/jfm.2026.11153 Published online by Cambridge University Press

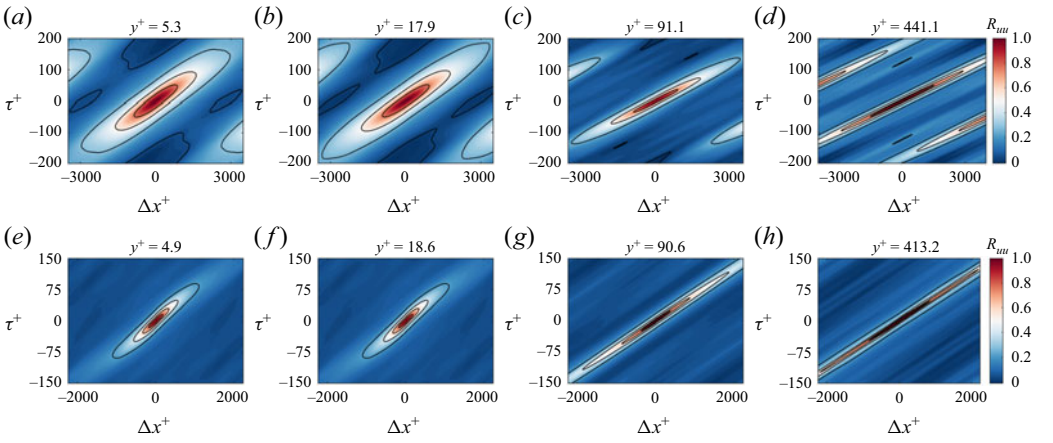


Figure 6. Contours of spatiotemporal correlation for the high-Mach-number cases M30R05k and M80R27k*: (*a–d*) M30R05k at (*a*) $y^+ = 5.3$, (*b*) $y^+ = 17.9$, (*c*) $y^+ = 91.1$, (*d*) $y^+ = 441.1$; (*e–h*) M80R27k* at (*e*) $y^+ = 4.9$, (*f*) $y^+ = 18.6$, (*g*) $y^+ = 90.6$, (*h*) $y^+ = 413.2$. Contours correspond to levels $R = 0.8,\ 0.6,\ 0.4,\ 0.2$.

1995). To test if ESS exists, we replot the temporal structure function as a function of the transformed variable r_x / V_c, where V_c is the characteristic velocity, which varies with y^+. Figure 5(*c*) compares the spatial and rescaled temporal structure functions. The strong alignment along the diagonal indicates that the two structure functions scale similarly when expressed in terms of a common variable – despite the breakdown of their classical inertial-range scalings. Invoking the ESS scalings and the random advection equation, another proof for the EA is detailed in Appendix B.

4.3. *Finite Mach numbers*

Classical issues in compressible flow have been extensively discussed and addressed in prior research, encompassing compressibility velocity transformations (Van Driest 1951; Trettel & Larsson 2016; Griffin, Fu & Moin 2021; Hasan *et al.* 2023), velocity–temperature relations (Walz 1969; Huang, Coleman & Bradshaw 1995; Zhang *et al.* 2014) and passive scalar statistics (Modesti & Pirozzoli 2019; Modesti, Pirozzoli & Grasso 2019). While most studies focus on one-point statistics, this work examines spatiotemporal correlations and assesses the validity of the EA in compressible channel flows, extending it to temperature fluctuations. The analysis expands the applicability of the EA to fluctuating Mach numbers up to 0.8, and for the first time, to the temperature field. Discussion centres on the two highest Mach number cases: M30R05k and M80R27k*. Results for intermediate Mach number cases (M08R03k and M15R03k) are documented in Appendix A.

4.3.1. *Velocity correlations*

Figure 6 shows spatiotemporal correlation contours for cases M30R05k and M80R27k* at four representative wall-normal locations each. The results are presented in wall-based ('+') units because the ellipticity of the correlation function – central to the EA model – is independent of the specific scaling. The slope of the principal axis of the contours reflects the convection velocity; thus an increase in convection velocity with wall-normal distance y^+ is observed. In M30R05k (figure 6*a–d*), the contours are approximately elliptical – more so than those at low Mach numbers, especially in the viscous sublayer ($y^+ = 5.3$, figure 6*a*). The contours become increasingly slender with distance from the wall, indicating more rapid decay in both autocorrelation $R(0, \tau)$ and cross-correlation $R(r, 0)$, consistent with trends seen under low-Mach-number conditions. A similar pattern

https://doi.org/10.1017/jfm.2026.11153 Published online by Cambridge University Press

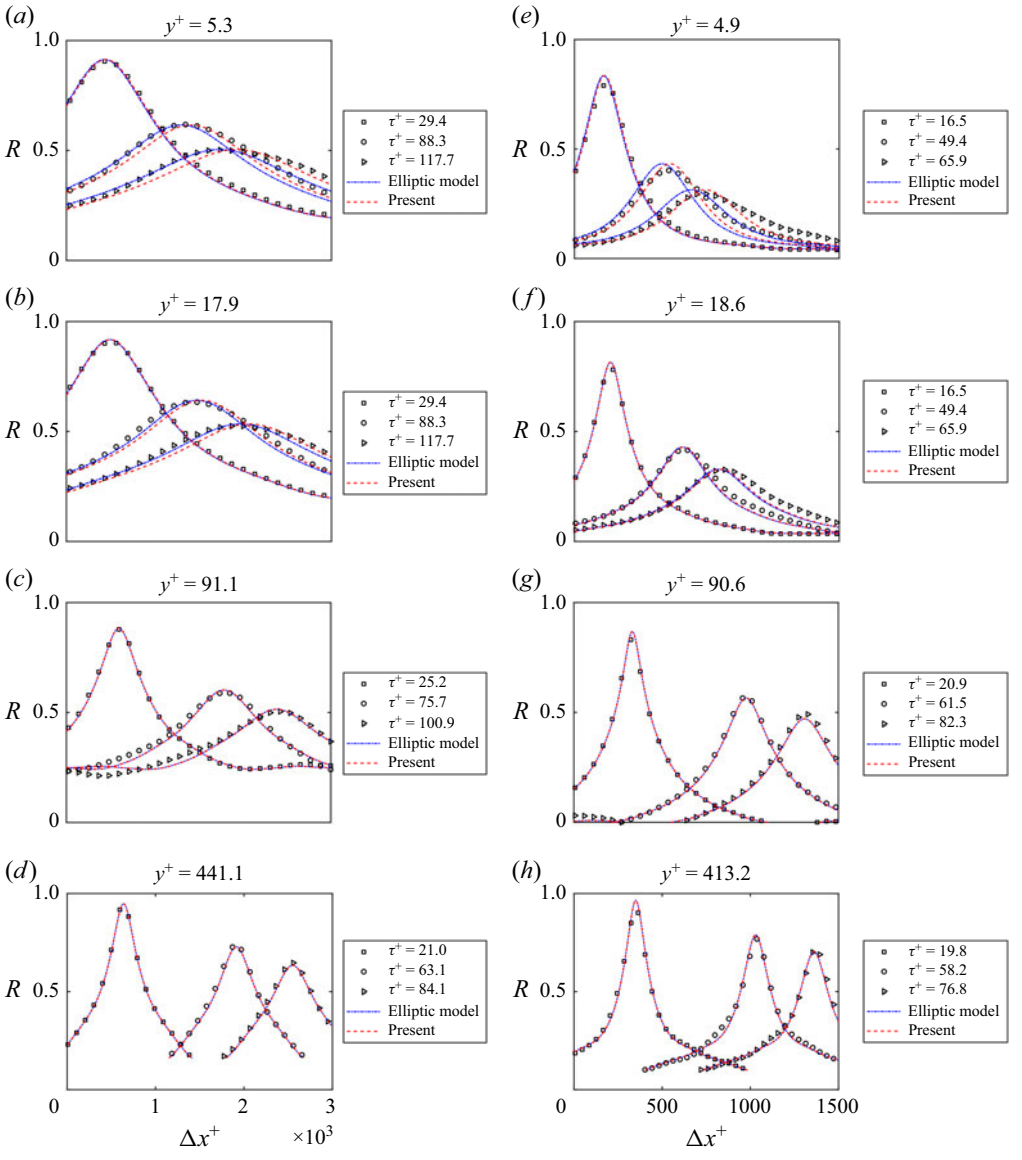


Figure 7. Comparison of spatiotemporal correlations from DNS (symbols) and reconstruction according to both the original EA with a constant convection velocity (dash-dotted lines) and a varying convection velocity that incorporates the shear-induced acceleration in (4.3) (dashed lines). (*a–d*) The high-Mach-number case M30R05k at (*a*) $y^+ = 5.3$, (*b*) $y^+ = 17.9$, (*c*) $y^+ = 91.1$, (*d*) $y^+ = 441.1$. (*e–h*) The high-Mach-number case M80R27k* at (*e*) $y^+ = 4.9$, (*f*) $y^+ = 18.6$, (*g*) $y^+ = 90.6$, (*h*) $y^+ = 413.2$.

is evident in M80R27k* (figure 6*e–h*), where the contours also retain an elliptical shape across all wall-normal positions.

To more rigorously assess the EA as given in (2.7), we reconstruct the space–time correlation profiles at selected time delays τ as functions of Δx^+. Reconstructions are performed according to both the original EA formulation with a constant convection velocity and the present model incorporating the shear-induced acceleration in (4.3). These reconstructions are compared with DNS results in figure 7. To minimise the influence of periodicity, the analysis focused on regions where the effects of the finite

https://doi.org/10.1017/jfm.2026.11153 Published online by Cambridge University Press

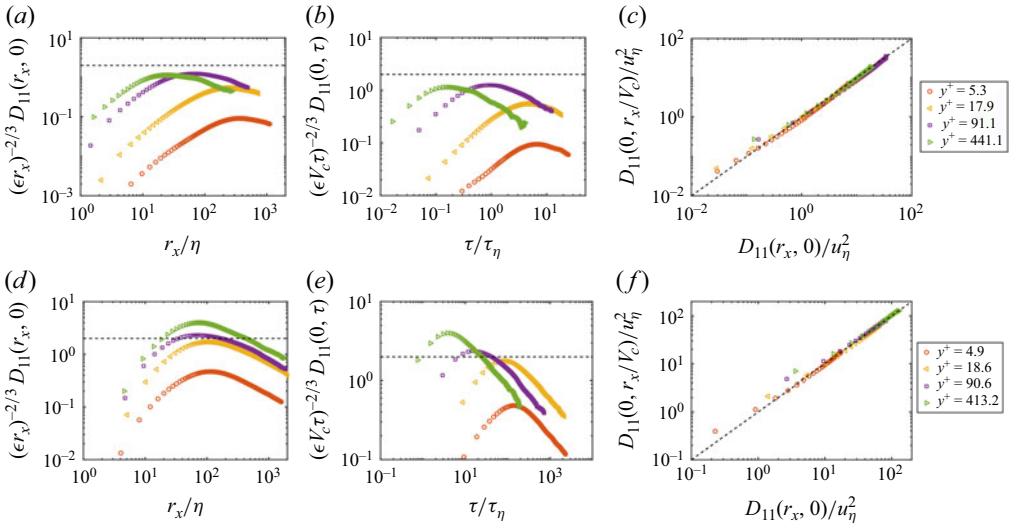


Figure 8. (*a–c*) Second-order structure functions for the high-Mach-number case M30R05k: (*a*) spatial structure function, compensated by $(\epsilon r_x)^{-2/3}$; (*b*) temporal structure function, compensated by $(\epsilon V_c \tau)^{-2/3}$; (*c*) temporal structure function plotted as a function of r_x/V_c against the spatial one. (*d–f*) Similarly for the high-Mach-number case M80R27k*.

domain size are negligible, as demonstrated in figures 7 and 10. For both M30R05k and M80R27k*, the reconstructed correlations match the DNS data closely across all wall-normal positions, with accuracy comparable to that achieved in incompressible flows (He & Zhang 2006; Zhao & He 2009). Minor discrepancies are found at large τ^+ near the wall. These, however, are effectively corrected by incorporating the modified convection velocity.

This result is somewhat surprising, as the current formulation does not distinguish between solenoidal and compressible components of the velocity field. While Wang *et al.* (2012) showed that solenoidal modes in compressible turbulence exhibit behaviour similar to incompressible turbulence, compressible modes display distinct dynamics characterised by fluctuations that propagate at the acoustic speed relative to the fluid. These dynamics usually need to be accounted for separately. For example, Lee, Lele & Moin (1992) proposed a linear wave propagation model for compressible velocity fluctuations, which was later extended by Li, Zhang & He (2013) to incorporate large-scale random sweeping effects. However, per the present result, the EA, despite being developed under the assumption of incompressibility, remains valid for fluctuating Mach numbers up to 0.8.

Next, we revisit the inertial-range assumptions in (2.9) and (2.10). Figure 8 presents the second-order velocity structure functions for cases M30R05k and M80R27k*, with figure 8(*a–c*) corresponding to M30R05k, and figure 8(*d–f*) to M80R27k*. The compensated plots of the spatial and temporal structure functions in figure 8(*a*,*b*,*d*,*e*) indicate that the inertial range is either narrow or absent in these cases. Despite this, figure 8(*c*,*f*) reveal the persistence of ESS: when temporal structure functions are plotted against their spatial counterparts using the characteristic velocity V_c, the data collapse onto a single curve. These results confirm that the validity of the EA in compressible turbulence does not rely on strict inertial-range scaling. Instead, it is supported by the more general and robust presence of ESS, consistent with findings in low-Mach-number flows.

https://doi.org/10.1017/jfm.2026.11153 Published online by Cambridge University Press

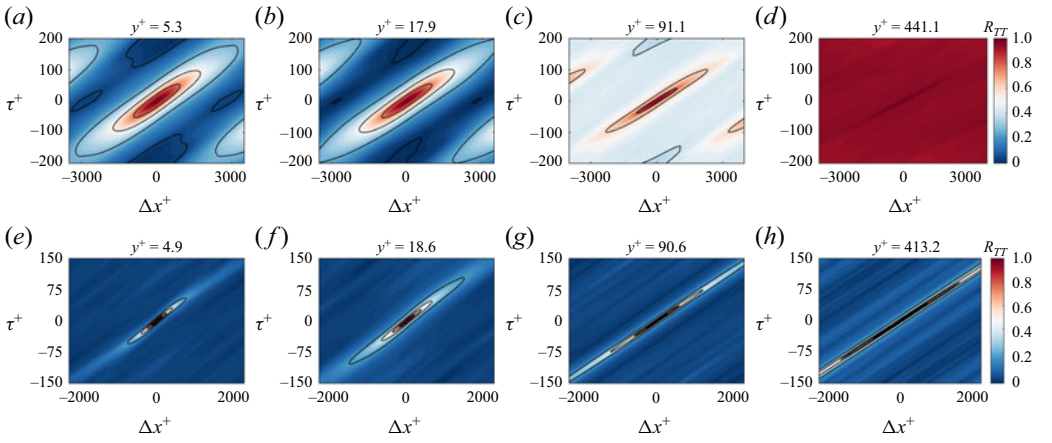


Figure 9. Contours of the temperature correlation function R_{TT} as a function of spatial separation and time delay. (*a–d*) The high-Mach-number case M30R05k at $y^+ = 5.3$, 17.9, 91.1, 441.1, respectively. (*e–h*) The high-Mach-number case M80R27k* at $y^+ = 4.9$, 18.6, 90.6, 413.2, respectively. Contours correspond to levels $R = 0.8,\ 0.6,\ 0.4,\ 0.2$.

4.3.2. *Temperature correlations*

In addition to velocity fluctuating, we also examine the spatiotemporal correlation of temperature fluctuations. Previous studies examining the applicability of the EA to temperature fluctuations focused primarily on incompressible regimes where temperature acts as a passive scalar (He *et al.* 2010; He & Tong 2011). However, the tenability of the EA for temperature fluctuations under finite Mach number remains an open question.

Figure 9 shows the temperature correlation contours R_{TT} for cases M30R05k and M80R27k* at four representative wall-normal positions. Figure 9(*a–d*) correspond to M30R05k. In the near-wall region ($y^+ = 5.3$, 17.9, figure 9*a*,*b*), the contours are elliptical, consistent with the assumptions of the EA. In contrast to other regions (figure 9*a*,*b*,*e–h*), correlations in the channel core of this case (figure 9*c*,*d*) decay notably slowly. This behaviour is attributed to the nearly uniform mean temperature profile near the centreline (see figure 1*b*), which suppresses temperature fluctuations despite vigorous turbulent mixing. In contrast, figure 9(*e–h*) show results for M80R27k*. The contours remain elliptical and exhibit no discernible bias across all wall-normal positions. A quantitative assessment of how closely these contours align with true ellipses is provided by the reconstruction results based on the EA model, as discussed in the subsequent section. Unlike M30R05k, M80R27k* maintains a significant mean temperature gradient even at the channel centre, sustaining strong temperature fluctuations and meaningful correlations throughout the domain.

To further assess the applicability of the EA, we reconstruct the temperature correlation function R_{TT} for both M30R05k and M80R27k* at selected time delays τ^+, using (2.7), and compare the results with DNS data in figure 10. Although the EA slightly underpredicts the peak correlation values, the overall agreement is strong, confirming that the EA effectively captures the spatiotemporal behaviour of temperature fluctuations in compressible turbulence.

The robustness of the EA for temperature is further supported by ESS. As in § 4.2, we examine the second-order temperature structure function, defined as

$$D_{TT}(r_x, \tau) = \left\langle \left| T'(x + r_x, t + \tau) - T'(x, t) \right|^2 \right\rangle, \tag{4.4}$$

https://doi.org/10.1017/jfm.2026.11153 Published online by Cambridge University Press

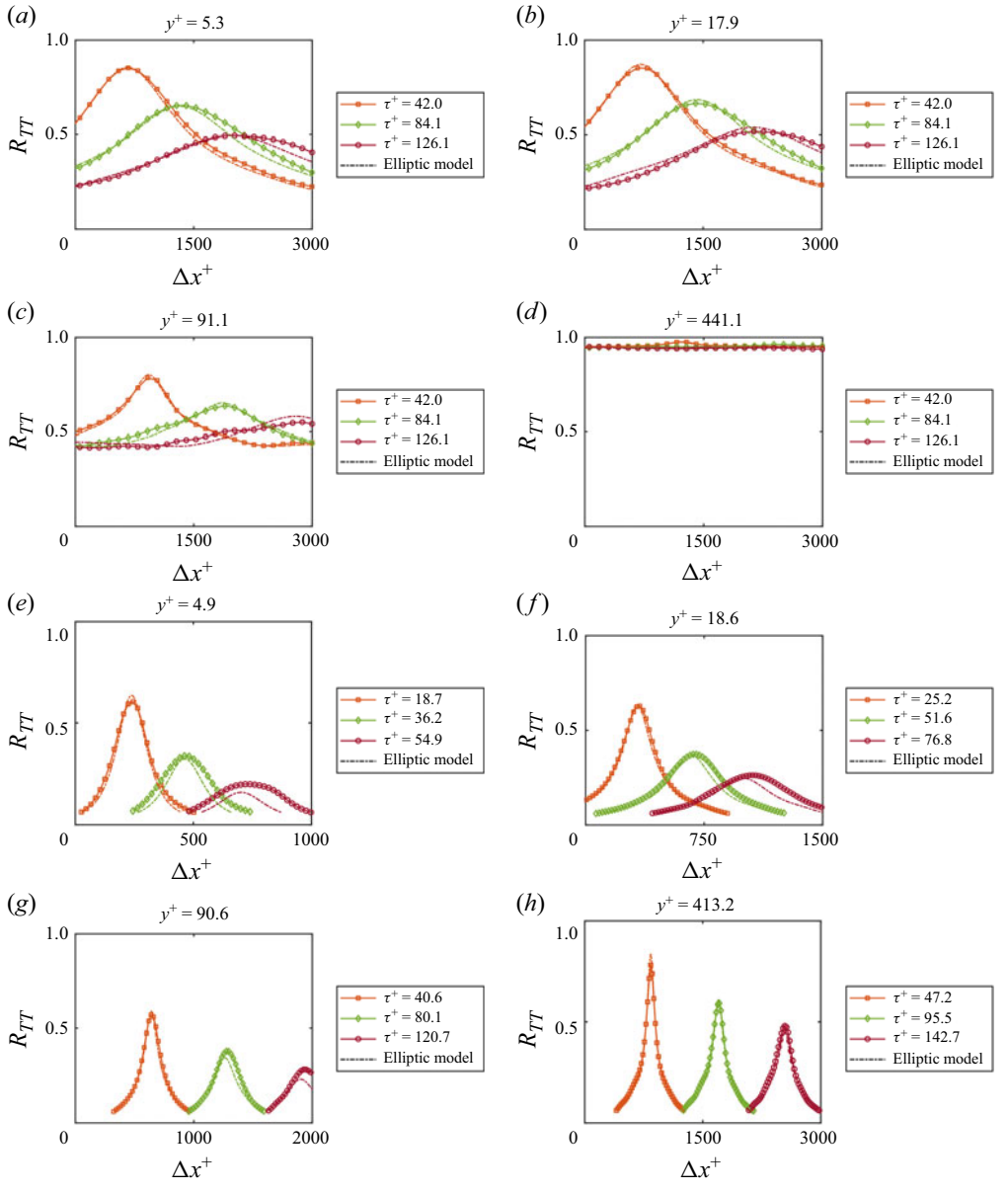


Figure 10. The DNS results (solid lines) and the reconstructions due to the EA (dash-dotted lines) of the temperature correlation function R_{TT} for the high-Mach-number case M30R05k at various wall-normal positions: (*a*) $y^+ = 5.3$, (*b*) $y^+ = 17.9$, (*c*) $y^+ = 91.1$, (*d*) $y^+ = 441.1$. The high-Mach-number case M80R27k* at (*e*) $y^+ = 4.9$, (*f*) $y^+ = 18.6$, (*g*) $y^+ = 90.6$, (*h*) $y^+ = 413.2$.

as shown in figure 11. Similar to the velocity case, the temperature structure functions have inertial-range scaling laws analogous to (2.9) and (2.10) (Antonia & Van Atta 1975; Antonia *et al.* 1996). The compensated structure functions are shown in figures 11(*a*,*b*) and 11(*d*,*e*), respectively. In both cases, the inertial-range plateau is narrow, indicating that the classical scaling laws are not strictly valid under the current flow conditions. However, ESS remains robust, as demonstrated in figure 11(*c*,*f*), where the temporal structure functions collapse when plotted against their spatial counterparts. These results confirm that despite

https://doi.org/10.1017/jfm.2026.11153 Published online by Cambridge University Press

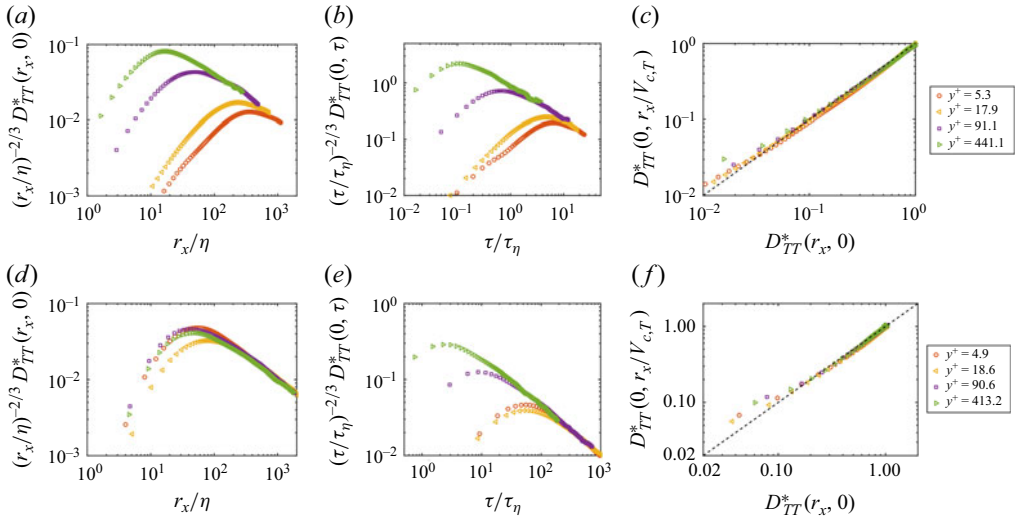


Figure 11. Second-order structure functions for temperature fluctuations. (*a–c*) Case M30R05k: (*a*) spatial structure function, compensated by $(r_x/\eta)^{-2/3}$; (*b*) temporal structure function, compensated by $(\tau/\tau_\eta)^{-2/3}$; (*c*) temporal temperature structure function plotted as a function of $(r_x/V_{c,T})$ against the spatial ones. Here, $V_{c,T}$ is the characteristic velocity related to temperature correlation function. (*d–f*) Case M80R27k*. The superscript $*$ denotes normalisation by $\langle T'T'\rangle$.

the absence of a clear inertial range, the presence of ESS supports the applicability of the EA to temperature fluctuations in compressible turbulent channel flows.

4.3.3. *Convection and sweeping velocities*

Finally, we examine the convection and sweeping velocities associated with the spatiotemporal correlations of both velocity and temperature fluctuations. According to the Reynolds analogy (Reynolds 1874), which links momentum and heat transport in turbulent flows, temperature and velocity fluctuations are expected to exhibit similar dynamical behaviour. This analogy implies that the spatiotemporal correlation functions R_{uu} and R_{TT} should have similar contour shapes, and identical convection and sweeping velocities. Figure 12 presents a comparison of the convection and sweeping velocities for temperature and velocity correlations. Figure 12(*a*) shows the convection velocities, denoted U for velocity correlation and U_T for temperature correlation. We also plot the mean velocity profiles for reference purposes. The focus is on the near-wall region, since in the logarithmic and outer layers, the convection velocity approaches the mean velocity. In the viscous sublayer and buffer layer, both U and U_T exceed the local mean velocity and are approximately equal to each other, except for some discrepancy in case M80R27k*. These convection velocities increase with Mach number. For example, in case M30R05k, the convection velocity remains nearly constant across the viscous sublayer at approximately $16u_\tau$, significantly higher than the typical incompressible value $\sim 10u_\tau$ (Geng *et al.* 2015). Besides, we observed that non-monotonic behaviours occurred in case M80R27k*, which has not been reported in previous work. Figure 12(*b*) displays the sweeping velocities, V for velocity and V_T for temperature. As with the convection velocities, V and V_T are nearly identical and also increase with Mach number. These results support the applicability of the EA to temperature fluctuations, consistent with the Reynolds analogy. They also align with the findings of He *et al.* (2010), who demonstrated the effectiveness of the EA in describing temperature correlations in Rayleigh–Bénard

https://doi.org/10.1017/jfm.2026.11153 Published online by Cambridge University Press

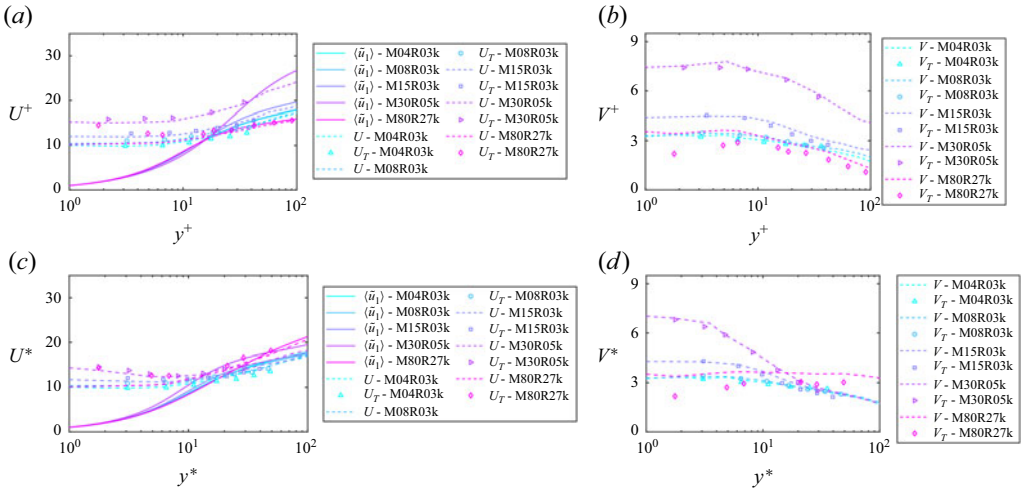


Figure 12. (*a*) Convection velocities for velocity and temperature correlations, denoted U and U_T, respectively. (*b*) Sweeping velocities, denoted V and V_T. (*c*) Convection velocities scaled by semi-local wall units for velocity and temperature correlations. (*d*) Sweeping velocities scaled by semi-local wall units.

convection. Although their study involved low-Mach-number flows where temperature acts as a passive scalar, the similarity in correlation dynamics remains evident. However, a discrepancy is observed in the near-wall region of case M80R27k*, potentially indicating a breakdown of the Reynolds analogy. This finding aligns with Yang *et al.* (2018), who demonstrated that the Reynolds analogy does not hold under conditions of significant aerodynamic heating. As previously established, such breakdown does not compromise the validity of the EA for temperature fluctuations in compressible flow. Figure 12(*c*,*d*) present the same convection and sweeping velocities scaled in semi-local wall units, defined as $u_\tau^* = \sqrt{\tau_w/\bar{\rho}}$ and $\delta_\nu^* = \bar{\nu}/u_\tau^*$. In figure 12(*c*), convection velocities show improved agreement with the low-Mach-number case M04R03k compared to those in figure 12(*a*). A similar trend is observed for the sweeping velocities in figure 12(*d*), where profiles away from the wall nearly collapse across cases – with the exception of M80R27k*. This general consistency aligns with the findings of Modesti & Pirozzoli (2016), who reported negligible compressibility effects on the spatial spectra with transformations, and those of Williams *et al.* (2018), who observed that the correlation length in hypersonic turbulent boundary layers decreases rather slowly as the Mach number increases.

5. Conclusion

This study revisits the theoretical foundation of the elliptic approximation (EA) and extends its applicability to compressible wall-bounded turbulence. The EA model, validated for the Mach number ranges investigated in this study, remains effective for both velocity and temperature fluctuations at supersonic conditions. It is important to note that while Taylor's hypothesis is a closely related concept, the present work does not directly bear upon its validity or the established criteria for its application.

We first identify the breakdown of the constant convection velocity assumption in the viscous sublayer, and propose a shear-induced acceleration correction that improves model accuracy at large time separations. Next, we show that the EA does not rely on classical inertial-range scalings, as originally derived from Kolmogorov's theory and the Kraichnan–Tennekes hypothesis. Instead, the model's validity is supported by the

https://doi.org/10.1017/jfm.2026.11153 Published online by Cambridge University Press

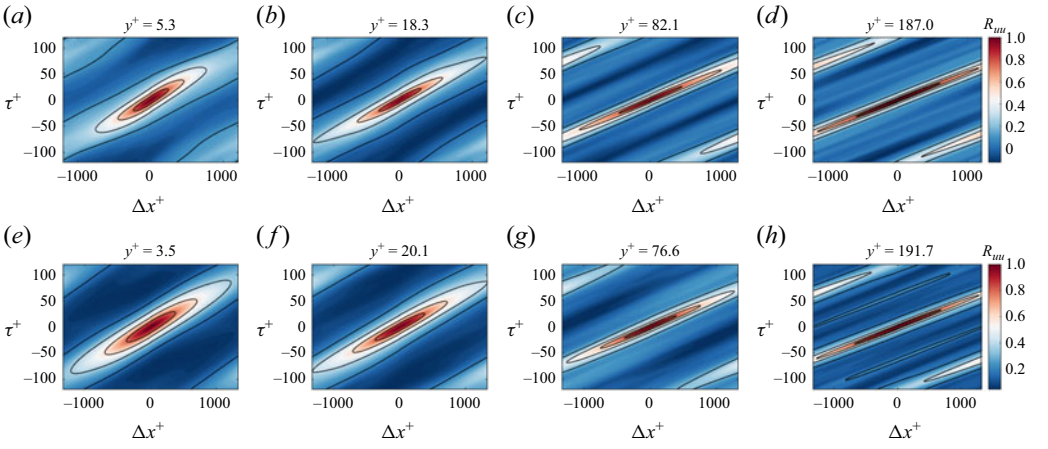


Figure 13. Contours of spatiotemporal correlation R for cases M08R03k and M15R03k. (*a–d*) Case M08R03k at (*a*) $y^+ = 5.3$, (*b*) $y^+ = 18.3$, (*c*) $y^+ = 82.1$, (*d*) $y^+ = 187.0$. (*e–h*) Case M15R03k at (*e*) $y^+ = 3.5$, (*f*) $y^+ = 20.1$, (*g*) $y^+ = 76.6$, (*h*) $y^+ = 191.7$. Contours correspond to levels $R = 0.8,\ 0.6,\ 0.4,\ 0.2$.

extended self-similarity between spatial and temporal structure functions, which holds even in the absence of a well-defined inertial range. Finally, our results demonstrate that the EA remains robust for both velocity and temperature correlations in compressible flows. These findings broaden the operational scope of the EA framework and provide new theoretical insights into the structure of compressible turbulence, offering a foundation for future modelling and experimental efforts in high-speed wall-bounded flows.

Declaration of interests. The authors report no conflict of interest.

Data availability statement. The data that support the findings of this study are available from the corresponding author upon reasonable request.

Appendix A. Additional results

The main text contains results for the low-Mach-number case M04R03k and the high-Mach-number cases M30R05k and M80R27k. This appendix presents results for the two intermediate Mach number cases: M08R03k and M15R03k. We will see that the results are similar to those at high Mach numbers. Figure 13 presents the spatiotemporal correlation contours of fluctuating velocity for M08R03k and M15R05k cases at four representavtive wall-normal locations each. The results are similar to those in figure 6. The reconstruction results of the original EA formulation with a constant convective velocity and our EA formulation with a varying convective velocity are shown in figure 14. The results are also similar to those in figure 7.

We also evaluate the space–time correlation of fluctuating temperature in figure 15. The results are similar to those in figure 9. We use the EA and our corrections to reconstruct the correlation function in figure 16.

Appendix B. Another proof of the EA model

In this appendix, we provide an alternative derivation of the EA model. We first present the derivation based on the classical random sweeping hypothesis with a globally constant sweeping velocity, as utilised by Wilczek & Narita (2012). We then extend this to a more general case, where the sweeping velocity varies in space and time.

https://doi.org/10.1017/jfm.2026.11153 Published online by Cambridge University Press

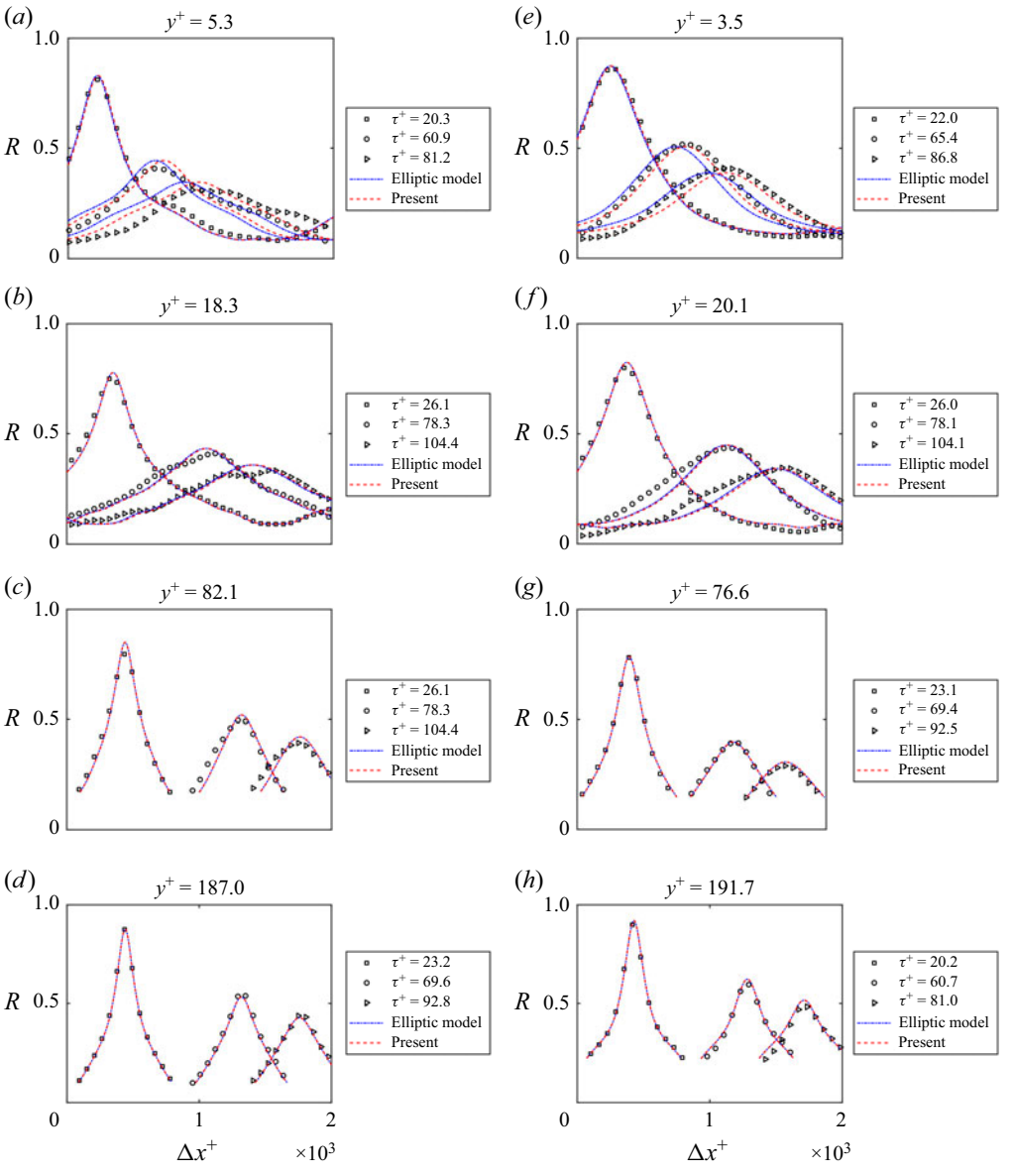


Figure 14. Comparison of spatiotemporal correlations R_{uu} from DNS (solid lines), the EA (dash-dotted lines), and our reformulation of the EA reconstructions (dashed lines). (*a–d*) Case M08R03k at (*a*) $y^+ = 5.3$, (*b*) $y^+ = 18.3$, (*c*) $y^+ = 82.1$, (*d*) $y^+ = 187.0$. (*e–h*) Case M15R03k at (*e*) $y^+ = 3.5$, (*f*) $y^+ = 20.1$, (*g*) $y^+ = 76.6$, (*h*) $y^+ = 191.7$.

As in Zhao & He (2009), we start by expanding the streamwise spatiotemporal correlation $R(r, \tau)$ around the origin to the second-order term:

$$R(r, \tau) = R(0, 0) + \frac{1}{2!}\left(r^2 \frac{\partial^2}{\partial r^2} + 2r\tau \frac{\partial^2}{\partial r\, \partial \tau} + \tau^2 \frac{\partial^2}{\partial \tau^2}\right) R\Big|_0, \tag{B1}$$

where $r \equiv r_1$ denotes the streamwise separation. By involving the random sweeping equation and ESS, we derive the necessary relationships between these second-order partial derivatives.

https://doi.org/10.1017/jfm.2026.11153 Published online by Cambridge University Press

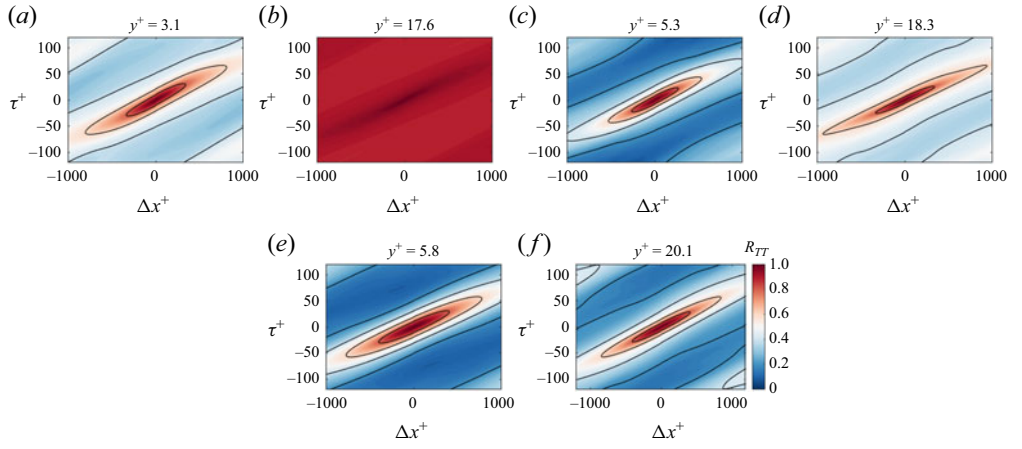


Figure 15. Contours of the temperature correlation function R_{TT} as a function of spatial separation and time delay. (*a,b*) Case M04R03k at $y^+ = 3.1$, 17.6, respectively. (*c,d*) Case M08R03k at $y^+ = 4.9$, 18.3, respectively. (*e,f*) Case M15R03k at $y^+ = 5.8$, 20.1, respectively. Contours correspond to levels $R =$ 0.8, 0.6, 0.4, 0.2.

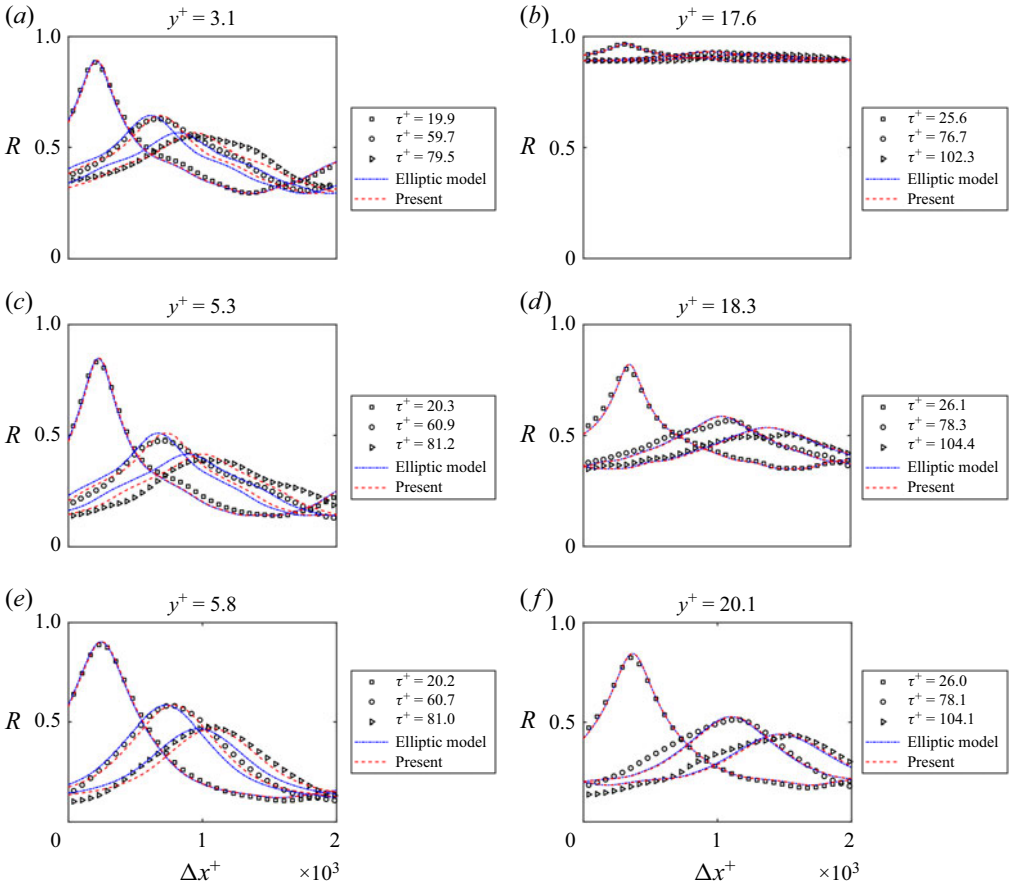


Figure 16. The DNS results (solid lines), reconstructions due to the EA (dash-dotted lines), and our reformulation of the EA (dashed lines) for the temperature correlation function R_{TT} for (*a,b*) case M04R03k at $y^+ = 3.1$, 17.6; (*c,d*) case M08R03k at $y^+ = 5.3$, 18.3; and (*e,f*) case M15R03k at $y^+ = 5.8$, 20.1.

https://doi.org/10.1017/jfm.2026.11153 Published online by Cambridge University Press

B.1. *Random sweeping with constant velocity*

Following the framework of Kraichnan (1964) and Wilczek & Narita (2012), one may assume that the random sweeping velocity $\boldsymbol{v}$ is constant in space and time for a given realisation, but varies across the ensemble with a Gaussian distribution. The advection equation for the fluctuating velocity $u_1(\boldsymbol{x}, t)$ is

$$\frac{\partial u_1}{\partial t} + (U_k + v_k)\frac{\partial u_1}{\partial x_k} = 0, \tag{B2}$$

where U_k is the mean convection velocity. Since $\boldsymbol{U}$ and $\boldsymbol{v}$ are constant for a single realisation, the exact solution is

$$u_1(\boldsymbol{x}, t) = u_1(\boldsymbol{x} - (\boldsymbol{U} + \boldsymbol{v})t, 0). \tag{B3}$$

To determine the space-time correlation $C(\boldsymbol{r}, \tau) = \langle u_1(\boldsymbol{x}', t)\, u_1(\boldsymbol{x}, 0)\rangle$ (where $\boldsymbol{x}' = \boldsymbol{x} + \boldsymbol{r}$ and $t = \tau$), we consider its derivative with respect to the time delay τ. When the separation vector $\boldsymbol{r}$ is aligned with the streamwise direction (i.e. $\boldsymbol{r} = r\boldsymbol{e}_1$), this function reduces to the streamwise spatiotemporal correlation $R(r, \tau)$ introduced earlier:

$$\frac{\partial C}{\partial \tau} = \left\langle \frac{\partial u_1(\boldsymbol{x}', t)}{\partial t}\, u_1(\boldsymbol{x}, 0)\right\rangle = -\left\langle (U_k + v_k)\,\frac{\partial u_1(\boldsymbol{x}', t)}{\partial x_k'}\, u_1(\boldsymbol{x}, 0)\right\rangle. \tag{B4}$$

Separating the mean and fluctuating parts yields

$$\frac{\partial C}{\partial \tau} = -U_k\frac{\partial C}{\partial r_k} - \frac{\partial}{\partial r_k}\langle v_k\, u_1(\boldsymbol{x}', t)\, u_1(\boldsymbol{x}, 0)\rangle. \tag{B5}$$

Since $\boldsymbol{v}$ is constant in individual ensemble members with a Gaussian distribution, its covariance is $\langle v_k v_j\rangle = V^2\delta_{kj}$. Furthermore, $\boldsymbol{v}$ is statistically independent of the initial field. Using Gaussian integration by parts,

$$\langle v_k\, F[\boldsymbol{v}]\rangle = \langle v_k v_j\rangle \left\langle \frac{\partial F}{\partial v_j}\right\rangle, \tag{B6}$$

with $F[\boldsymbol{v}] = u_1(\boldsymbol{x}', t)\, u_1(\boldsymbol{x}, 0)$ depending on $\boldsymbol{v}$, the last term in (B5) becomes

$$\begin{aligned}\langle v_k\, u_1(\boldsymbol{x}', t)\, u_1(\boldsymbol{x}, 0)\rangle &= \langle v_k v_j\rangle \left\langle \frac{\partial u_1(\boldsymbol{x}', t) u_1(\boldsymbol{x}, 0)}{\partial v_j}\right\rangle \\ &= \langle v_k v_j\rangle \left\langle \frac{\partial u_1(\boldsymbol{x}', t)}{\partial v_j} u_1(\boldsymbol{x}, 0) + u_1(\boldsymbol{x}', t)\frac{\partial u_1(\boldsymbol{x}, 0)}{\partial v_j}\right\rangle \\ &= V^2\left\langle \frac{\partial u_1(\boldsymbol{x}', t)}{\partial v_k} u_1(\boldsymbol{x}, 0) + u_1(\boldsymbol{x}', t)\frac{\partial u_1(\boldsymbol{x}, 0)}{\partial v_k}\right\rangle.\end{aligned} \tag{B7}$$

From the exact solution of the advection (B3), the response functions are

$$\frac{\partial u_1(\boldsymbol{x}', t)}{\partial v_k} = -t\frac{\partial u_1(\boldsymbol{x}', t)}{\partial x_k'} \quad \text{and} \quad \frac{\partial u_1(\boldsymbol{x}, 0)}{\partial v_k} = 0. \tag{B8}$$

Substituting (B7) and (B8) back into the correlation (B5) leads to

$$\frac{\partial C}{\partial \tau} + U_k\frac{\partial C}{\partial r_k} = V^2\tau\frac{\partial^2 C}{\partial r_k\,\partial r_k}. \tag{B9}$$

This is an advection–diffusion equation with a time-dependent diffusivity $V^2\tau$. The solution to this equation corresponds to the convolution of the spatial correlation with a Gaussian kernel.

https://doi.org/10.1017/jfm.2026.11153 Published online by Cambridge University Press

B.2. *Generalised random sweeping with space–time dependence*

In the present work, we consider a more general case where the incompressible random sweeping velocity field $v_i(\boldsymbol{x}', t)$ depends on both space and time. The governing equation involves the spatially varying sweeping field:

$$\frac{\partial u_1(\boldsymbol{x}', t)}{\partial t} + U_j \frac{\partial u_1(\boldsymbol{x}', t)}{\partial x_j'} + \frac{\partial}{\partial x_j'} \left(v_j(\boldsymbol{x}', t)\, u_1(\boldsymbol{x}', t) \right) = 0. \tag{B10}$$

Multiplying by $u_1(\boldsymbol{x}, 0)$ and ensemble averaging yields

$$\frac{\partial \left\langle u_1(\boldsymbol{x}', t)\, u_1(\boldsymbol{x}, 0) \right\rangle}{\partial t} + U_j \frac{\partial \left\langle u_1(\boldsymbol{x}', t)\, u_1(\boldsymbol{x}, 0) \right\rangle}{\partial x_j'} + \left\langle \frac{\partial \left(v_j(\boldsymbol{x}', t)\, u_1(\boldsymbol{x}', t)\, u_1(\boldsymbol{x}, 0) \right)}{\partial x_j'} \right\rangle = 0, \tag{B11}$$

with the closure term for the sweeping effect

$$\Pi_j = \left\langle v_j(\boldsymbol{x}', t)\, u_1(\boldsymbol{x}', t)\, u_1(\boldsymbol{x}, 0) \right\rangle. \tag{B12}$$

We apply the Furutsu–Novikov theorem (Furutsu 1963; Novikov 1965) assuming v_j is a Gaussian process:

$$\Pi_j = \int_0^\infty \mathrm{d}\theta \int_\Omega \mathrm{d}\boldsymbol{z} \left\langle v_j(\boldsymbol{x}', t)\, v_k(\boldsymbol{z}, \theta) \right\rangle \left\langle \frac{\delta[u_1(\boldsymbol{x}', t)\, u_1(\boldsymbol{x}, 0)]}{\delta v_k(\boldsymbol{z}, \theta)} \right\rangle. \tag{B13}$$

The variables $\boldsymbol{z}$ and θ represent the spatial and temporal integration variables, respectively. The functional derivative term decomposes into

$$\left\langle \frac{\delta[u_1(\boldsymbol{x}', t)\, u_1(\boldsymbol{x}, 0)]}{\delta v_k(\boldsymbol{z}, \theta)} \right\rangle = \left\langle \frac{\delta u_1(\boldsymbol{x}', t)}{\delta v_k(\boldsymbol{z}, \theta)} u_1(\boldsymbol{x}, 0) + u_1(\boldsymbol{x}', t) \frac{\delta u_1(\boldsymbol{x}, 0)}{\delta v_k(\boldsymbol{z}, \theta)} \right\rangle. \tag{B14}$$

The second term vanishes since at $t = 0$, u_1 is statistically independent of $\boldsymbol{v}$ at future time. To determine the response function, we take the variation of (B10) with respect to $v_k(\boldsymbol{z}, \theta)$:

$$\frac{\delta}{\delta v_k(\boldsymbol{z}, \theta)} \left[\frac{\partial u_1(\boldsymbol{x}', t)}{\partial t} + U_j \frac{\partial u_1(\boldsymbol{x}', t)}{\partial x_j'} + v_j(\boldsymbol{x}', t) \frac{\partial u_1(\boldsymbol{x}', t)}{\partial x_j'} \right] = 0, \tag{B15}$$

which could be written as

$$\left[\frac{\partial}{\partial t} + U_j \frac{\partial}{\partial x_j'} + v_j(\boldsymbol{x}', t) \frac{\partial}{\partial x_j'} \right] \left[\frac{\delta u_1(\boldsymbol{x}', t)}{\delta v_k(\boldsymbol{z}, \theta)} \right] = - \frac{\delta v_j(\boldsymbol{x}', t)}{\delta v_k(\boldsymbol{z}, \theta)} \frac{\partial u_1(\boldsymbol{x}', t)}{\partial x_j'}, \tag{B16}$$

where the right-hand side is equal to

$$- \frac{\delta v_j(\boldsymbol{x}', t)}{\delta v_k(\boldsymbol{z}, \theta)} \frac{\partial u_1(\boldsymbol{x}', t)}{\partial x_j'} = -\delta_{kj}\, \delta(\boldsymbol{x}' - \boldsymbol{z})\, \delta(t - \theta) \frac{\partial u_1(\boldsymbol{x}', t)}{\partial x_j'}. \tag{B17}$$

Then we get

$$\left[\frac{\partial}{\partial t} + U_j \frac{\partial}{\partial x_j'} + v_j(\boldsymbol{x}', t) \frac{\partial}{\partial x_j'} \right] \left[\frac{\delta u_1(\boldsymbol{x}', t)}{\delta v_k(\boldsymbol{z}, \theta)} \right] = -\delta_{kj}\, \delta(\boldsymbol{x}' - \boldsymbol{z})\, \delta(t - \theta) \frac{\partial u_1(\boldsymbol{x}', t)}{\partial x_j'}. \tag{B18}$$

We introduce the quasi-linear approximation. This approximation is justified when $\epsilon = \sqrt{\langle v_i v_i \rangle}/|\boldsymbol{U}|$ is small. For small ϵ, the term $v_j\, \partial_{x_j'}$ in the governing equation is negligible

https://doi.org/10.1017/jfm.2026.11153 Published online by Cambridge University Press

compared to $U_j\,\partial_{x_j'}$, thus the higher-order interaction between the fluctuating sweeping velocity can be neglected. Equation (B18) simplifies to

$$\left[\frac{\partial}{\partial t}+U_j\frac{\partial}{\partial x_j'}\right]\left[\frac{\delta u_1(\boldsymbol{x}',t)}{\delta v_k(\boldsymbol{z},\theta)}\right]=-\delta_{kj}\,\delta(\boldsymbol{x}'-\boldsymbol{z})\,\delta(t-\theta)\frac{\partial u_1(\boldsymbol{x}',t)}{\partial x_j'}. \tag{B19}$$

Multiplying (B19) by the velocity $u_1(\boldsymbol{x},0)$, and taking the ensemble average, yields

$$\left[\frac{\partial}{\partial t}+U_j\frac{\partial}{\partial x_j'}\right]\left\langle\frac{\delta u_1(\boldsymbol{x}',t)}{\delta v_k(\boldsymbol{z},\theta)}u_1(\boldsymbol{x},0)\right\rangle=-\delta_{kj}\,\delta(\boldsymbol{x}'-\boldsymbol{z})\,\delta(t-\theta)\left\langle\frac{\partial u_1(\boldsymbol{x}',t)}{\partial x_j'}u_1(\boldsymbol{x},0)\right\rangle. \tag{B20}$$

This is a convection equation featuring a source term in δ form, whose solution can be expressed as

$$\left\langle\frac{\delta u_1(\boldsymbol{x}',t)}{\delta v_k(\boldsymbol{z},\theta)}u_1(\boldsymbol{x},0)\right\rangle=-\left\langle\frac{\partial u_1(\boldsymbol{x}',t)}{\partial x_k'}u_1(\boldsymbol{x},0)\right\rangle H(t-\theta)\,\delta(\boldsymbol{x}'-\boldsymbol{z}-\boldsymbol{U}(t-\theta)), \tag{B21}$$

where H is the Heaviside step function, ensuring causal behaviour in the solution ($t>\theta$). Substituting (B21) into (B13), we have

$$\begin{aligned}\Pi_j=&-\int_0^{+\infty}\mathrm{d}\theta\int_\Omega\mathrm{d}\boldsymbol{z}\,\langle v_j(\boldsymbol{x}',t)\,v_k(\boldsymbol{z},\theta)\rangle\left\langle\frac{\partial u_1(\boldsymbol{x}',t)}{\partial x_k'}u_1(\boldsymbol{x},0)\right\rangle\\&\times H(t-\theta)\,\delta\left(\boldsymbol{x}'-\boldsymbol{z}-\boldsymbol{U}(t-\theta)\right).\end{aligned} \tag{B22}$$

By applying the variable substitution $s=\theta-t$ and $\boldsymbol{\Delta}=\boldsymbol{z}-\boldsymbol{x}'$, and using $H(t-\theta)$, which restricts $\theta\in[0,t]$, the integral reduces to

$$\begin{aligned}\Pi_j&=-\left\langle\frac{\partial u_1(\boldsymbol{x}',t)}{\partial x_k'}u_1(\boldsymbol{x},0)\right\rangle\int_{-t}^{+\infty}\mathrm{d}s\int_\Omega C_{v_kv_j}(\boldsymbol{\Delta},s)\,H(-s)\,\delta\,(\boldsymbol{\Delta}-\boldsymbol{U}s)\,\mathrm{d}\boldsymbol{\Delta}\\&=-\left\langle\frac{\partial u_1(\boldsymbol{x}',t)}{\partial x_k'}u_1(\boldsymbol{x},0)\right\rangle\int_{-t}^{0}C_{v_kv_j}(\boldsymbol{U}s,s)\,\mathrm{d}s\\&=-\Gamma_{kj}\frac{\partial C}{\partial r_k},\end{aligned} \tag{B23}$$

where $C_{v_kv_j}(\boldsymbol{\Delta},s)=\langle v_k(\boldsymbol{z},\theta)\,v_j(\boldsymbol{x}',t)\rangle$ is the correlation function of the sweeping velocity field. The formulation assumes that the velocity statistics are homogeneous and stationary. The resulting diffusivity tensor $\Gamma_{kj}(\tau)$ is obtained by integrating the correlation along the characteristic line defined by the mean velocity $\boldsymbol{U}$:

$$\int_{-\tau}^{0}C_{v_kv_j}(\boldsymbol{U}s,s)\,\mathrm{d}s. \tag{B24}$$

Substituting (B23) into (B11), we arrive at the generalised transport equation:

$$\frac{\partial C}{\partial\tau}+U_j\frac{\partial C}{\partial r_j}=\Gamma_{kj}\frac{\partial^2 C}{\partial r_j\,\partial r_k}. \tag{B25}$$

Note that if we treat the sweeping velocity as a constant per realisation (as in § B.1), then the correlation function $C_{v_kv_j}$ does not decay, and $\Gamma_{kj}=\int_{-\tau}^{0}\langle v_kv_j\rangle\,\mathrm{d}s=V^2\tau\delta_{kj}$, which is consistent with the results of § B.1. To derive the relations between second-order partial

https://doi.org/10.1017/jfm.2026.11153 Published online by Cambridge University Press

derivatives, we differentiate (B25) with respect to r_1:

$$\frac{\partial^2 C}{\partial r_1\,\partial \tau}=\frac{\partial}{\partial r_1}\left[\frac{\partial C}{\partial \tau}\right]=\frac{\partial}{\partial r_1}\left[(-U)\frac{\partial C}{\partial r_1}+\Gamma_{kj}\frac{\partial^2 C}{\partial r_k\,\partial r_j}\right]=(-U)\frac{\partial^2 C}{\partial r_1^2}+\Gamma_{kj}\frac{\partial^3 C}{\partial r_1\,\partial r_k\,\partial r_j}. \tag{B26}$$

When evaluating this equation at the origin ($\boldsymbol{r}=\boldsymbol{0}$, $\tau=0$), the second term on the right-hand side vanishes. This is due to $\Gamma_{kj}(\tau)=\int_{-\tau}^{0} C_{v_k v_j}(\boldsymbol{U}s, s)\,\mathrm{d}s$, so $\Gamma_{kj}(0)$ equals zero. Consequently, we obtain

$$\left.\frac{\partial^2 R}{\partial r_1\,\partial \tau}\right|_0=\left.\frac{\partial^2 C}{\partial r_1\,\partial \tau}\right|_0=-U\left.\frac{\partial^2 C}{\partial r_1^2}\right|_0=-U\left.\frac{\partial^2 R}{\partial r_1^2}\right|_0. \tag{B27}$$

Next, we invoke the ESS scaling:

$$R(V_c\tau, 0)=R(0, \tau). \tag{B28}$$

We take the derivative with respect to τ:

$$(V_c)^2\frac{\partial^2 R}{\partial r^2}=\frac{\partial^2 R}{\partial \tau^2}. \tag{B29}$$

Substituting (B27) and (B29) into (B1), we have

$$\begin{aligned}R(r,\tau)&=R(0,0)+\frac{1}{2!}\left(r^2\frac{\partial^2}{\partial r^2}-2Ur\tau\frac{\partial^2}{\partial r^2}+V_c^2\tau^2\frac{\partial^2}{\partial r^2}\right)R\Big|_0\\&=R(0,0)+\frac{1}{2!}\left[\frac{\partial^2}{\partial r^2}\left((r^2-2Ur\tau+U^2\tau^2)+(V_c^2-U^2)\tau^2\right)\right]R\Big|_0\\&=R(0,0)+\frac{1}{2!}\left(\frac{\partial^2}{\partial r^2}r_c^2\right)R\Big|_0\\&=R(r_c,0).\end{aligned} \tag{B30}$$

Here, $r_c^2=((r-U\tau)^2+(V\tau)^2)$, which is the EA, and $V^2=V_c^2-U^2$ represents the contribution of random sweeping to the spatiotemporal decorrelation.

References

Antonia, R.A. & Van Atta, C.W. 1975 On the correlation between temperature and velocity dissipation fields in a heated turbulent jet. *J. Fluid Mech.* **67** (2), 273–288.

Antonia, R.A., Zhu, Y., Anselmet, F. & Ould-Rouis, M. 1996 Comparison between the sum of second-order velocity structure functions and the second-order temperature structure function. *Phys. Fluids* **8** (11), 3105–3111.

Atkinson, C., Buchmann, N.A. & Soria, J. 2015 An experimental investigation of turbulent convection velocities in a turbulent boundary layer. *Flow Turbul. Combust.* **94**, 79–95.

Benzi, R., Ciliberto, S., Baudet, C. & Chavarria, G.R. 1995 On the scaling of three-dimensional homogeneous and isotropic turbulence. *Phys. D: Nonlinear Phenom.* **80** (4), 385–398.

Benzi, R., Ciliberto, S., Tripiccione, R., Baudet, C., Massaioli, F. & Succi, S. 1993 Extended self-similarity in turbulent flows. *Phys. Rev. E* **48** (1), R29.

Bogey, C. & Bailly, C. 2004 A family of low dispersive and low dissipative explicit schemes for flow and noise computations. *J. Comput. Phys.* **194** (1), 194–214.

Cambon, C. & Scott, J.F. 1999 Linear and nonlinear models of anisotropic turbulence. *Annu. Rev. Fluid. Mech.* **31** (1), 1–53.

Chen, P.E.S., Huang, G.P., Shi, Y., Yang, X.I.A. & Lv, Y. 2022 A unified temperature transformation for high-Mach-number flows above adiabatic and isothermal walls. *J. Fluid Mech.* **951**, A38.

Chen, P.E.S., Zhu, X., Shi, Y. & Yang, X.I.A. 2023 Quantifying uncertainties in direct-numerical-simulation statistics due to wall-normal numerics and grids. *Phys. Rev. Fluids* **8** (7), 074602.

https://doi.org/10.1017/jfm.2026.11153 Published online by Cambridge University Press

COLEMAN, G.N., KIM, J. & MOSER, R.D. 1995 A numerical study of turbulent supersonic isothermal-wall channel flow. *J. Fluid Mech.* **305**, 159–183.

DEL ALAMO, J.C. & JIMÉNEZ, J. 2009 Estimation of turbulent convection velocities and corrections to Taylor's approximation. *J. Fluid Mech.* **640**, 5–26.

DENNIS, D.J.C. & NICKELS, T.B. 2008 On the limitations of Taylor's hypothesis in constructing long structures in a turbulent boundary layer. *J. Fluid Mech.* **614**, 197–206.

DUAN, L., BEEKMAN, I. & MARTIN, M.P. 2011 Direct numerical simulation of hypersonic turbulent boundary layers. Part 3. Effect of Mach number. *J. Fluid Mech.* **672**, 245–267.

FAVRE, A. 1965 Review on space–time correlations in turbulent fluids. *J. Appl. Mech.* **32** (2), 241–257.

FLORES, O. & JIMÉNEZ, J. 2010 Hierarchy of minimal flow units in the logarithmic layer. *Phys. Fluids* **22** (7), 071704.

FURUTSU, K. 1963 On the statistical theory of electromagnetic waves in a fluctuating medium. *J. Res. Natl Bur. Stand. D* **67**, 303–323.

GENG, C., HE, G., WANG, Y., XU, C., LOZANO-DURÁN, A. & WALLACE, J.M. 2015 Taylor's hypothesis in turbulent channel flow considered using a transport equation analysis. *Phys. Fluids* **27** (2), 025111.

GRIFFIN, K.P., FU, L. & MOIN, P. 2021 Velocity transformation for compressible wall-bounded turbulent flows with and without heat transfer. *Proc. Natl Acad. Sci. USA* **118** (34), e2111144118.

HASAN, A.M., LARSSON, J., PIROZZOLI, S. & PECNIK, R. 2023 Incorporating intrinsic compressibility effects in velocity transformations for wall-bounded turbulent flows. *Phys. Rev. Fluids* **8** (11), L112601.

HE, G., JIN, G. & YANG, Y. 2017 Space–time correlations and dynamic coupling in turbulent flows. *Annu. Rev. Fluid. Mech.* **49** (1), 51–70.

HE, G.-W. & ZHANG, J.-B. 2006 Elliptic model for space–time correlations in turbulent shear flows. *Phys. Rev. E* **73** (5), 055303.

HE, X., HE, G. & TONG, P. 2010 Small-scale turbulent fluctuations beyond Taylor's frozen-flow hypothesis. *Phys. Rev. E* **81** (6), 065303.

HE, X. & TONG, P. 2011 Kraichnan's random sweeping hypothesis in homogeneous turbulent convection. *Phys. Rev. E* **83** (3), 037302.

HE, X. & TONG, P. 2014 Space–time correlations in turbulent Rayleigh–Bénard convection. *Acta Mechanica Sin.* **30**, 457–467.

HUANG, J., DUAN, L. & CHOUDHARI, M.M. 2022 Direct numerical simulation of hypersonic turbulent boundary layers: effect of spatial evolution and Reynolds number. *J. Fluid Mech.* **937**, A3.

HUANG, P.G., COLEMAN, G.N. & BRADSHAW, P. 1995 Compressible turbulent channel flows: DNS results and modelling. *J. Fluid Mech.* **305**, 185–218.

HUTCHINS, N., NICKELS, T.B., MARUSIC, I. & CHONG, M.S. 2009 Hot-wire spatial resolution issues in wall-bounded turbulence. *J. Fluid Mech.* **635**, 103–136.

KIM, J., MOIN, P. & MOSER, R. 1987 Turbulence statistics in fully developed channel flow at low Reynolds number. *J. Fluid Mech.* **177**, 133–166.

KOLMOGOROV, A.N. 1941 The local structure of turbulence in incompressible viscous fluid for very large Reynolds numbers. *Dokl. Akad. Nauk SSSR* **30**, 301.

KOLMOGOROV, A.N. 1991 Dissipation of energy in the locally isotropic turbulence. *Proc. R. Soc. Lond. A: Math. Phys. Sci.* **434** (1890), 15–17.

KRAICHNAN, R.H. 1961 Dynamics of nonlinear stochastic systems. *J. Math. Phys.* **2** (1), 124–148.

KRAICHNAN, R.H. 1964 Kolmogorov's hypotheses and Eulerian turbulence theory. *Phys. Fluids* **7** (11), 1723–1734.

KRISTENSEN, L. 1979 On longitudinal spectral coherence. *Boundary-Layer Meteorol.* **16** (2), 145–153.

LEE, S., LELE, S.K. & MOIN, P. 1992 Simulation of spatially evolving turbulence and the applicability of Taylor's hypothesis in compressible flow. *Phys. Fluids* **4** (7), 1521–1530.

LI, D., ZHANG, X. & HE, G. 2013 Temporal decorrelations in compressible isotropic turbulence. *Phys. Rev. E* **88** (2), 021001.

LI, X.-L., FU, D.-X. & MA, Y.-W. 2006 Direct numerical simulation of a spatially evolving supersonic turbulent boundary layer at Ma = 6. *Chin. Phys. Lett.* **23** (6), 1519.

LI, X.-L., FU, D.-X., MA, Y.-W. & LIANG, X. 2010 Direct numerical simulation of compressible turbulent flows. *Acta Mechanica Sin.* **26** (6), 795–806.

LIANG, X. & LI, X. 2015 Direct numerical simulation on Mach number and wall temperature effects in the turbulent flows of flat-plate boundary layer. *Commun. Comput. Phys.* **17** (1), 189–212.

LIGHTHILL, M.J. 1952 On sound generated aerodynamically. I. General theory. *Proc. R. Soc. Lond. A: Math. Phys. Sci.* **211** (1107), 564–587.

LIGRANI, P.M. & BRADSHAW, P. 1987 Spatial resolution and measurement of turbulence in the viscous sublayer using subminiature hot-wire probes. *Exp. Fluids.* **5** (6), 407–417.

https://doi.org/10.1017/jfm.2026.11153 Published online by Cambridge University Press

LOZANO-DURÁN, A. & JIMÉNEZ, J. 2014 Effect of the computational domain on direct simulations of turbulent channels up to $Re_\tau = 4200$. *Phys. Fluids* **26** (1), 011702.
LUKASSEN, L.J., STEVENS, R.J.A.M., MENEVEAU, C. & WILCZEK, M. 2018 Modeling space–time correlations of velocity fluctuations in wind farms. *Wind Energy* **21** (7), 474–487.
MANN, J. 1994 The spatial structure of neutral atmospheric surface-layer turbulence. *J. Fluid Mech.* **273**, 141–168.
DE MARÉ, M. & MANN, J. 2016 On the space–time structure of sheared turbulence. *Boundary-Layer Meteorol.* **160** (3), 453–474.
MODESTI, D., BERNARDINI, M. & PIROZZOLI, S. 2015 High-Reynolds-number effects on turbulent scalings in compressible channel flow. *Proc. Appl. Maths Mech.* **15** (1), 489–490.
MODESTI, D. & PIROZZOLI, S. 2016 Reynolds and Mach number effects in compressible turbulent channel flow. *Intl J. Heat Mass Transfer* **59**, 33–49.
MODESTI, D. & PIROZZOLI, S. 2019 Direct numerical simulation of supersonic pipe flow at moderate Reynolds number. *Intl J. Heat Fluid Flow* **76**, 100–112.
MODESTI, D., PIROZZOLI, S. & GRASSO, F. 2019 Direct numerical simulation of developed compressible flow in square ducts. *Intl J. Heat Fluid Flow* **76**, 130–140.
MOIN, P. 2009 Revisiting Taylor's hypothesis. *J. Fluid Mech.* **640**, 1–4.
MORINISHI, Y., TAMANO, S. & NAKABAYASHI, K. 2004 Direct numerical simulation of compressible turbulent channel flow between adiabatic and isothermal walls. *J. Fluid Mech.* **502**, 273–308.
NOVIKOV, E.A. 1965 Functionals and the random-force method in turbulence theory. *Sov. Phys. JETP* **20** (5), 1290–1294.
OLIVER, T.A., MALAYA, N., ULERICH, R. & MOSER, R.D. 2014 Estimating uncertainties in statistics computed from direct numerical simulation. *Phys. Fluids* **26** (3), 035101.
ORSZAG, S.A. 1973 Statistical theory of turbulence. *Fluid Dyn.* 237–374.
PHILLIPS, W.R.C. 2000 Eulerian space–time correlations in turbulent shear flows. *Phys. Fluids* **12** (8), 2056–2064.
POPE, S.B. 2001 Turbulent flows. *Meas. Sci. Technol.* **12** (11), 2020–2021.
REYNOLDS, O. 1874 On the extent and action of the heating surface of steam boilers. *Proc. Lit. Phil. Soc. Manchester* **14**, 7–12.
SANADA, T. & SHANMUGASUNDARAM, V. 1992 Random sweeping effect in isotropic numerical turbulence. *Phys. Fluids* **4** (6), 1245–1250.
TAYLOR, G.I. 1938 The spectrum of turbulence. *Proc. R. Soc. Lond. A: Math. Phys. Sci.* **164** (919), 476–490.
TENNEKES, H. 1975 Eulerian and Lagrangian time microscales in isotropic turbulence. *J. Fluid Mech.* **67** (3), 561–567.
TOWNE, A., LOZANO-DURÁN, A. & YANG, X. 2020 Resolvent-based estimation of space–time flow statistics. *J. Fluid Mech.* **883**, A17.
TRETTEL, A. & LARSSON, J. 2016 Mean velocity scaling for compressible wall turbulence with heat transfer. *Phys. Fluids* **28** (2), 026102.
VAN, D. & EDWARD, R. 1951 Turbulent boundary layer in compressible fluids. *J. Aeronaut. Sci.* **18** (3), 145–160.
VUKOSLAVČEVIĆ, P., WALLACE, J.M. & BALINT, J.-L. 1991 The velocity and vorticity vector fields of a turbulent boundary layer. Part 1. Simultaneous measurement by hot-wire anemometry. *J. Fluid Mech.* **228**, 25–51.
WALLACE, J.M. 2014 Space–time correlations in turbulent flow: a review. *Theor. Appl. Mech. Lett.* **4** (2), 022003.
WALZ, A. 1969 *Boundary Layers of Flow and Temperature*. MIT Press.
WANG, J., SHI, Y., WANG, L.-P., XIAO, Z., HE, X.T. & CHEN, S. 2012 Effect of compressibility on the small-scale structures in isotropic turbulence. *J. Fluid Mech.* **713**, 588–631.
WANG, M., FREUND, J.B. & LELE, S.K. 2006 Computational prediction of flow-generated sound. *Annu. Rev. Fluid Mech.* **38** (1), 483–512.
WANG, W., GUAN, X.-L. & JIANG, N. 2014 TRPIV investigation of space–time correlation in turbulent flows over flat and wavy walls. *Acta Mechanica Sin.* **30** (4), 468–479.
WILCZEK, M. & NARITA, Y. 2012 Wave-number–frequency spectrum for turbulence from a random sweeping hypothesis with mean flow. *Phys. Rev. E* **86** (6), 066308.
WILCZEK, M., STEVENS, R.J.A.M. & MENEVEAU, C. 2015*a* Height-dependence of spatio-temporal spectra of wall-bounded turbulence – LES results and model predictions. *J. Turbul.* **16** (10), 937–949.
WILCZEK, M., STEVENS, R.J.A.M. & MENEVEAU, C. 2015*b* Spatio-temporal spectra in the logarithmic layer of wall turbulence: large-eddy simulations and simple models. *J. Fluid Mech.* **769**, R1.
WILLIAMS, O.J.H., SAHOO, D., BAUMGARTNER, M.L. & SMITS, A.J. 2018 Experiments on the structure and scaling of hypersonic turbulent boundary layers. *J. Fluid Mech.* **834**, 237–270.

https://doi.org/10.1017/jfm.2026.11153 Published online by Cambridge University Press

WILLS, J.A.B. 1964 On convection velocities in turbulent shear flows. *J. Fluid Mech.* **20** (3), 417–432.
WU, T. & HE, G. 2021*a* Space–time energy spectra in turbulent shear flows. *Phys. Rev. Fluids* **6** (10), 100504.
WU, T. & HE, G. 2021*b* Stochastic dynamical model for space–time energy spectra in turbulent shear flows. *Phys. Rev. Fluids* **6** (5), 054602.
XU, D., WANG, J., WAN, M., YU, C., LI, X. & CHEN, S. 2021 Effect of wall temperature on the kinetic energy transfer in a hypersonic turbulent boundary layer. *J. Fluid Mech.* **929**, A33.
YANG, B., JIN, G., WU, T., YANG, Z. & HE, G. 2020 Numerical implementation and evaluation of resolvent-based estimation for space–time energy spectra in turbulent channel flows. *Acta Mechanica Sin.* **36**, 775–788.
YANG, B. & YANG, Z. 2022 On the wavenumber–frequency spectrum of the wall pressure fluctuations in turbulent channel flow. *J. Fluid Mech.* **937**, A39.
YANG, X.I.A., HONG, J., LEE, M. & HUANG, X.L.D. 2021 Grid resolution requirement for resolving rare and high intensity wall-shear stress events in direct numerical simulations. *Phys. Rev. Fluids* **6** (5), 054603.
YANG, X.I.A., URZAY, J., BOSE, S. & MOIN, P. 2018 Aerodynamic heating in wall-modeled large-eddy simulation of high-speed flows. *AIAA J.* **56** (2), 731–742.
YAO, J. & HUSSAIN, F. 2020 Turbulence statistics and coherent structures in compressible channel flow. *Phys. Rev. Fluids* **5** (8), 084603.
YU, M. & XU, C.-X. 2021 Compressibility effects on hypersonic turbulent channel flow with cold walls. *Phys. Fluids* **33** (7), 075106.
YU, M., XU, C.-X. & PIROZZOLI, S. 2019 Genuine compressibility effects in wall-bounded turbulence. *Phys. Rev. Fluids* **4** (12), 123402.
YU, M., XU, C.-X. & PIROZZOLI, S. 2020 Compressibility effects on pressure fluctuation in compressible turbulent channel flows. *Phys. Rev. Fluids* **5** (11), 113401.
ZHANG, C., DUAN, L. & CHOUDHARI, M.M. 2018 Direct numerical simulation database for supersonic and hypersonic turbulent boundary layers. *AIAA J.* **56** (11), 4297–4311.
ZHANG, P., SONG, Y. & XIA, Z. 2023 Compressibility effect in compressible turbulent channel flows. *Sci. Sin. Phys. Mech. Astronom.* **53** (4), 244711.
ZHANG, P.-J.-Y., WAN, Z.-H. & SUN, D.-J. 2019 Space–time correlations of velocity in a Mach 0.9 turbulent round jet. *Phys. Fluids* **31** (11), 115108.
ZHANG, Y.-S., BI, W.-T., HUSSAIN, F. & SHE, Z.-S. 2014 A generalized Reynolds analogy for compressible wall-bounded turbulent flows. *J. Fluid Mech.* **739**, 392–420.
ZHAO, X. & HE, G.-W. 2009 Space–time correlations of fluctuating velocities in turbulent shear flows. *Phys. Rev. E* **79** (4), 046316.
ZHOU, Q., LI, C.-M., LU, Z.-M. & LIU, Y.-L. 2011 Experimental investigation of longitudinal space–time correlations of the velocity field in turbulent Rayleigh–Bénard convection. *J. Fluid Mech.* **683**, 94–111.

https://doi.org/10.1017/jfm.2026.11153 Published online by Cambridge University Press